Evolution of material voids for highly anisotropic surface energy

M. Siegel[a,*], M.J. Miksis[b], P.W. Voorhees[c]

[a] *Department of Mathematical Sciences, New Jersey Institute of Technology, Newark, NJ 07102, USA*
[b] *Engineering Sciences and Applied Mathematics, Northwestern University, Evanston, IL 67606, USA*
[c] *Department of Material Science and Engineering, Northwestern University, Evanston, IL 67606, USA*

Abstract

In this paper we consider the evolution by surface diffusion of material voids in a linearly elastic solid, focusing on the evolution of voids with large surface energy anisotropy. It is well known that models for the time evolution of similar material surfaces can become mathematically ill-posed when the surface energy is highly anisotropic. In some cases, this ill-posedness has been associated with the formation of corners along the interface. Here the ill-posedness is removed through a regularization which incorporates higher order terms in the surface energy. Spectrally accurate numerical simulations are performed to calculate the steady-state solution branches and time-dependent evolution of voids, with a particular emphasis on inferring trends in the zero regularization ($c \rightarrow 0$) limit. For steady voids with large anisotropy we find that apparent corners form as $c \rightarrow 0$. In the presence of elastic stresses σ the limiting corner angles are most often found to differ from angles found on the ($\sigma = 0$) Wulff shape. For large elastic stresses we find that steady solutions no longer exist; instead the void steadily lengthens via a filamenting instability referred to as tip streaming.
© 2003 Elsevier Ltd. All rights reserved.

1. Introduction

Surface roughening of materials caused by elastic stress is now recognized to be an important mechanism for the formation of islands in strained epitaxial films as well as the appearance of cracks and defects in solids. Interest in surface roughening has

---

* Corresponding author. Tel.: +1-973-596-5835; fax: +1-973-596-6467.
  E-mail address: misieg@impulse.njit.edu (M. Siegel).

been spurred by early studies (Asaro and Tiller, 1972; Grinfeld, 1986; Srolovitz, 1989) showing that a flat surface bounding a semi-infinite elastic solid is unstable to small amplitude shape perturbations, as long as the wavelength of the perturbation is sufficiently large. The instability results from the competition between elastic strain energy, which tends to destabilize the interface, and surface energy, which has a stabilizing influence. Early investigations mainly considered mass transport of atoms by surface diffusion, although the instability is qualitatively similar for other mass transport mechanisms (Srolovitz, 1989). The stability analyses have been extended to include the case of an epitaxially strained thin solid film on a substrate (Spencer et al., 1991; Freund and Jonsdottir, 1993), which has important applications in semi-conductor technology. A review of theoretical and experimental investigations on surface roughening and related topics is given in Gao and Nix (1999), Shchukin and Bimberg (1999), and Gao (1994).

More recent investigations of the late time, non-linear stages of the interface morphology reveal some interesting aspects. Chiu and Gao (1993) have analytically calculated the total energy for materials bounded by a one parameter family of cycloid shapes. They show that the total energy decreases as the cycloid sharpens, suggesting that a truly cusped shape is energetically favorable under certain conditions. Numerical studies by Spencer and Meiron (1994) and Yang and Srolovitz (1994) on periodically perturbed surfaces bounding a semi-infinite solid indicate that sharp, cusp like features emerge when the initial perturbation is of sufficiently large wavelength. Such behavior is interpreted as being a mechanism by which a smooth interface can form a crack front. In addition, experiments (Jesson et al., 1993; Ozkan et al., 1997) suggest that stress concentration near cusp tips can aid in the nucleation of dislocations in a previously defect free film or solid. Surface roughening can also lead to island formation in a strained film when the troughs touch the substrate (Kutka and Freund, 1997; Spencer and Tersoff, 1997; Zhang and Bower, 1999).

Studies of the evolution of voids in elastic solids have been performed in tandem with these efforts, and have revealed similar behavior. Gao (1991, 1992) applied perturbation techniques to demonstrate morphological instability for stressed voids above a critical radius. The energy calculation described above for cycloids was generalized to a set of closed shapes known as hypocycloids in Gao (1995). Hypocycloid cusps are found to be energetically favorable for large enough (unperturbed) radius. Full numerical calculations of void evolution using a conformal map based boundary integral method (Wang and Suo, 1997) and a finite element method (Xia et al., 1997) provide evidence that cusps do indeed form during the time-dependent evolution for pore radii above the critical value. These results have possible ramifications in the failure of microelectronic circuits (Arzt et al., 1994).

Clearly, the crystalline nature of materials leads to anisotropy of physical quantities, such as surface energy, which must be taken into account in theoretical studies. All of the studies described above have considered either isotropic surface energy or surfaces with weakly anisotropic surface energy (defined more precisely below). For particles or voids with weak surface energy anisotropy and in the absence of elastic strain energy, the equilibrium shapes are smooth curves given by the well-known Wulff construction. However, *highly* anisotropic surface energy leads to complications in the description of both the equilibrium shapes and time evolving surfaces, as is now described.

The motion of free surfaces in materials is driven by variations in a chemical potential along the surface. One component of the chemical potential, denoted μ_s, is related to the surface energy γ. For crystals with anisotropic surface energy γ is normally taken to be a function only of the orientation angle θ, defined to be the angle of the outward surface normal n with respect to the x-axis. In this case, the contribution of the anisotropic surface energy to the chemical potential is described by the well-known relation (Herring, 1951)

$$\mu_s = \mu_s^o + \Omega[\gamma(\theta) + \gamma''(\theta)]\kappa, \tag{1}$$

where μ_s^o is the chemical potential at a flat surface, κ is the interfacial curvature, considered positive for a convex profile, Ω is the atomic volume, and the prime denotes derivative with respect to θ. A representative expression for $\gamma(\theta)$ used throughout this paper is that for a simple four-fold symmetry

$$\gamma(\theta) \equiv \gamma_1 = \gamma_0[1 + \varepsilon \cos 4(\theta - \theta_0)], \tag{2}$$

where ε is a measure of the degree of anisotropy, γ_0 is the mean interfacial tension, and θ_0 gives the angle of maximum surface energy.

The θ dependence of μ_s described in (1), (2) leads to severe difficulties when $\varepsilon > 1/15$. In that case there exists values of the angle θ for which the expression

$$\gamma_1 + \gamma_1'' = \gamma_0[1 - 15\varepsilon \cos 4(\theta - \theta_0)] \tag{3}$$

is less than zero. (Following convention, such angles will be referred to as unstable orientations; angles for which expression (3) is non-negative are called stable or metastable orientations.) At unstable orientations, the coefficient in front of the largest derivative term in the equation governing evolution (see (7)) is negative, and the initial value problem is ill-posed. Additionally, exact equilibrium solutions (Burton et al., 1951; Mullins, 1962) corresponding to surfaces of constant chemical potential (see (1)) show that the steady (Wulff) shapes of unstressed voids subject to large anisotropy have 'missing orientations', i.e., corners with jumps in θ along the surface (see Voorhees et al., 1984, for plots of the Wulff shapes associated with (2) for a range of ε; or refer to Figs. 6 and 7 of this paper for sample profiles with missing orientations).

There are two ways of overcoming the ill-posedness associated with the existence of angles with $\gamma + \gamma'' < 0$. One is to eliminate the unstable angles by requiring the existence of corners. This approach is discussed in detail for the case of unstressed solids in Angenant and Gurtin (1989) (see also Gurtin, 1993), and stressed solids in Gurtin and Voorhees (1998). In either case, a force balance argument shows that the *admissible* corner angles for an evolving interface with surface energy density satisfying (2) are uniquely determined by ε, and in fact are the equilibrium corner angles on the Wulff shape Note that the insistence on corners seems to preclude the possibility of cusp formation, since a cusp necessarily contains unstable angles. A 'regularization' of the ill-posedness in unstressed solids, in a way which is consistent with the assumption of local equilibrium at corners but which is more suitable for numerical computation, is discussed in Eggleston et al. (2001). There a convexified energy density $\gamma^*(\theta)$ is employed for which $\gamma^{*''}(\theta) + \gamma^*(\theta) \geqslant 0$. The convexified energy density leads to the same equilibrium corner angles as the original surface energy density, but does

not in itself produce ill-posed evolution. Phase field numerical simulations (Eggleston et al., 2001) show that an initial interface containing angles for which $\gamma + \gamma'' < 0$ will quickly wrinkle into a faceted shape with only stable orientations. One disadvantage of this approach is that even with the convexified energy function, it is not possible to follow the evolution of an unstable orientation in a physically meaningful manner when elastic stress is present, due to stress induced ill-posedness at orientations where $\gamma^{*''}(\theta) + \gamma^*(\theta) = 0$.

A second approach is to regularize the evolution equations by incorporating curvature dependence in the surface energy, an idea that goes back to Gibbs (1878) and Herring (1951). Dynamical equations for interface controlled evolution with a curvature dependent interfacial energy first appeared in Angenent and Gurtin (1979) (see also DiCarlo et al., 1992). Related studies are Stewart and Goldenfeld (1992), Liu and Metiu (1993), and Golovin et al. (1998). This paper contains the first study of stress effects on the formation of corner angles in the zero regularization limit. Specifically, we consider the steady-state morphology and time-dependent evolution for a void in a stressed solid focusing on the evolution for large anisotropy. The regularized governing equations are introduced in Section 2. In Section 3 we reformulate the governing equations in terms of a conformal map. The approach is similar to Wang and Suo (1997), although we provide a different derivation of the governing equations which leads to a more compact form, and which is easily generalized to include the regularization. This formulation is particularly convenient for numerical computation in cases when cusps form on the interface, as well as computation of steady-state solutions. Unfortunately, the conformal map formulation does not fare well for long-time (unsteady) computations with non-zero regularization, one reason being the presence of numerical stiffness that is introduced due to the existence of high-order regularization terms. Therefore, we provide an alternative formulation based on an arclength–angle variables, which enables an efficient treatment of the stiffness. Numerical results are presented in Section 4, with a particular focus on the steady-state morphology and time-dependent evolution in the limit of zero regularization. Some discussion and concluding remarks are presented in Section 5.

2. Mathematical formulation

Our formulation follows Spencer and Meiron (1994) (see also Wang and Suo, 1997; Xia et al., 1997) with appropriate changes introduced to account for the differing geometry and the inclusion of anisotropic surface energy with regularization. Consider a simply connected void embedded in an infinite two-dimensional solid. The solid region is denoted by D, with boundary ∂D, and the void region is represented by D'. The relation between stress and strain in the solid is assumed to be given by Hooke's law for an isotropic material. Anisotropy in our study is incorporated solely in the surface energy, i.e., we neglect anisotropy in the elastic fields. This is the simplest way to add anisotropic effects, and reflects the expectation that surface anisotropy is more important than the volumetric elastic anisotropy. It is further assumed that the void contains vapor maintained at a stress state $T_{ij} = P\delta_{ij}$, where T_{ij} are components

of the stress tensor for $i, j, = 1, 2$, δ_{ij} is the unit tensor, and P is a constant. The corresponding constant strain state is chosen as a reference for the measurement of strains. Stress deviations from this constant state are denoted by σ_{ij}.

The governing equations for the elasticity problem are simply stated. Mechanical equilibrium within the solid requires that the stress tensor be divergence free, i.e.,

$$\partial_j \sigma_{ij} = 0 \quad \text{for } (x_1, x_2) \in D, \tag{4}$$

where ∂_j denotes the partial derivative with respect to coordinate x_j. At the surface of the void it is supposed that the tractions are small compared to the bulk stresses and can therefore be neglected. This leads to the zero traction boundary condition

$$\sigma_{ij} n_j = 0, \tag{5}$$

where n_j indicates the jth component of the outward unit normal to the surface. Finally, far from the void a state of biaxial stress is imposed

$$\sigma_{ij} = \begin{pmatrix} \sigma_1 & 0 \\ 0 & \sigma_2 \end{pmatrix} \quad \text{as } \sqrt{x_1^2 + x_2^2} \to \infty. \tag{6}$$

Eqs. (4)–(6) determine the stress distribution throughout the solid for a given interface.

We next discuss the kinematic equation governing the motion of the void surface. The boundary of the void is allowed to evolve via surface mass transport under the influence of a chemical potential. We shall neglect bulk transport (see Mullins, 1963). According to the Einstein–Nernst relation, the diffusional flux of atoms is proportional to the surface gradient of the chemical potential; by mass conservation the rate at which material is deposited or removed form the void surface equals the (negative) divergence of the surface flux. Thus (see Mullins, 1957),

$$V_n = \frac{D}{\Omega} \frac{\partial^2 \mu}{\partial^2 s}, \tag{7}$$

where $V_n(s, t)$ is the instantaneous velocity of the void surface in the direction of the outward normal, s is arclength measured in the clockwise direction, and D is a diffusion constant with units of volume/(energy density · time).

The kinematical description is completed by specifying the dependence of chemical potential on surface quantities, i.e., on interfacial shape and stress distribution. The chemical potential is decomposed as

$$\mu = \mu_0 + \mu_s + \mu_e, \tag{8}$$

where μ_0 is a constant reference potential, μ_s is the contribution to the chemical potential coming from surface energy, and μ_e is the contribution coming from the elastic strain energy. Following our earlier remarks we introduce a regularization by adding high-order terms to μ_s. The regularization is given a physical justification following arguments (Golovin et al., 1998) for an interface below the roughening transition. We imagine the surface energy of the crystal to be associated with the energy of (microscopic) steps on the crystal surface (Nozieres, 1992). Define θ to be the orientation angle of the macroscopic crystal surface. It is clear that taking γ to be a function only of θ is equivalent to taking the step energy to be a function only

of the local number density n of steps. More precisely, for a uniform set of steps n satisfies the relation $n = \tan \theta / \lambda$, where λ is the step height. However, at points where the interface curvature is high the surface varies rapidly, implying that dn/ds is large. In this case it is more appropriate to consider the surface energy not only as a function of n but also of $dn/ds = \kappa/(\lambda \cos^2 \theta)$. We therefore take $\gamma = \gamma(\theta, \kappa)$ for the thermodynamically rough interfaces considered here. Alternatively, the curvature dependence of the surface energy represents the energy associated with corners and edges.

The contribution of the surface energy to the chemical potential μ_s is then obtained by minimizing $E = \int \gamma(\theta, \kappa) \, ds$ over volume preserving variations of the interface. Upon forming the Euler–Lagrange equations for this minimization problem and identifying the chemical potential with the Lagrange multiplier (Mullins, 1963; Coriell and Sekerka, 1976) one obtains [1]

$$\mu_s = \left[\gamma + \frac{\partial^2 \gamma}{\partial \theta^2} - \kappa \left(1 + \frac{d^2}{d\theta^2} \right) \frac{\partial \gamma}{\partial \kappa} - \frac{\partial^2 \gamma}{\partial \kappa^2} \left(\frac{d\kappa}{d\theta} \right)^2 \right] \kappa. \tag{9}$$

Details of the derivation are given in Golovin et al. (1998) and, from a different perspective, Di Carlo et al. (1992). As in Di Carlo et al. (1992), Liu and Metiu (1993) and Golovin et al. (1998), we describe the dependence of γ on curvature by the simple expression

$$\gamma(\theta, \kappa) = \gamma_1(\theta) + \frac{c_1}{2} \kappa^2, \tag{10}$$

where c_1 is a constant and $\gamma_1(\theta)$ is the anisotropic surface tension corresponding to an oriented plane (low curvature) surface, as given in (2). The factor of two is chosen for convenience.

The other main component of the chemical potential is the term μ_e derived from considerations of the elastic strain energy density. This term takes the form (see e.g., Spencer and Meiron, 1994)

$$\mu_e = -\Omega \omega, \tag{11}$$

where

$$\omega = \frac{1 - v^2}{2E} (\sigma_{11} + \sigma_{22})^2 \tag{12}$$

is the strain energy density evaluated at the interface, i.e., $\sigma_{11} + \sigma_{22}$ is evaluated at the surface. Here E is Young's modulus and v is Poisson's ratio. It is noted that this expression assumes plain strain elasticity. Eqs. (4)–(12) comprise the complete statement of our problem and are the main result of this section.

---

[1] It is algebraically simpler to perform the minimization in Cartesian (x–y) coordinates by writing the dependence on orientation and curvature as $\gamma(h_x, h_{xx})$ for a surface given by $h(x)$, and then to transform to polar coordinates. See Golovin et al. (1998).

2.1. Non-dimensionalization

The governing equations stated above can be recast in terms of non-dimensional quantities if we rescale σ_{ij} by σ_1, ω by σ_1^2/E, γ by the mean interfacial tension γ_0, lengths by a (the undeformed pore radius) and time by $a^4/(D\gamma_0)$. The dimensionless surface energy is then given by (in this section dimensionless quantities are indicated by a tilde)

$$\tilde{\gamma} = \tilde{\gamma}_1 + \frac{\tilde{c}}{2}\,\tilde{\kappa}^2,$$

where $\tilde{\gamma}_1 = 1 + \varepsilon\cos 4(\theta - \theta_0)$ and $\tilde{c} = c_1/(\gamma_0 a^2)$ specifies the level of regularization. In terms of non-dimensional quantities the kinematic relation (7) takes the form

$$\tilde{V}_n = \frac{\partial^2}{\partial\tilde{s}^2}\left\{[\tilde{\gamma}_1 + \tilde{\gamma}_1'']\tilde{\kappa} - \tilde{c}\left(\frac{\tilde{\kappa}^3}{2} + \frac{\partial^2\tilde{\kappa}}{\partial\tilde{s}^2}\right) - \Lambda\tilde{\omega}\right\}, \tag{13}$$

where

$$\Lambda = \frac{2\sigma_1^2 a(1 - v^2)}{E\gamma_0} \tag{14}$$

measures the relative importance of elastic energy to surface energy. In deriving (13) we have used expression (9), which in turn is simplified by employing (10) and the identity $\theta_s = -\kappa$. The non-dimensional strain energy density is given by

$$\tilde{\omega} = \tfrac{1}{4}(\tilde{\sigma}_{11} + \tilde{\sigma}_{22})^2. \tag{15}$$

Eqs. (4) and (5) governing the elasticity problem are trivially modified into non-dimensional form. Finally, the far-field condition (6) is expressed as

$$\tilde{s}_{ij} = \begin{pmatrix} 1 & 0 \\ 0 & \chi \end{pmatrix} \quad \text{as} \quad \sqrt{\tilde{x}_1^2 + \tilde{x}_2^2} \to \infty, \tag{16}$$

where the dimensionless variable $\chi = \sigma_2/\sigma_1$ has been introduced. In the following sections we drop the tildes, with the understanding that all variables are dimensionless.

3. Reformulation of governing equations

We employ two complementary numerical methods in our study of void evolution. One method is based on a conformal map parameterization of the interface and is particularly well suited to computations when the interface develops sharp cusp-like features, as is the case when regularization is absent. The reason is that a zero angled cusp corresponds to a zero of the derivative of the map rather than blow up in a derivative, and may be resolved with a relatively few discretization points. However, this method is not efficient for long time computations in the case $c > 0$, for reasons which are discussed in Section 3.2. Consequently, for $c > 0$ long time computations are implemented using a boundary integral method based on an arclength–angle representation of the interface.

In this section the governing equations of Section 2 are reformulated in a way which allows the two methods to be readily introduced.

3.1. Complex variable formulation

We first consider a complex variable formulation of the governing equations. Introduce the conformal map $z(\zeta, t)$ which maps the interior of the unit circle in the ζ plane to the material region exterior to the void. The map may be decomposed as

$$z(\zeta, t) = \frac{a_0(t)}{\zeta} + h(\zeta, t),$$

where $a_0(t)$ can be chosen real and positive as allowed by the Riemann Mapping Theorem. The function $h(\zeta, t)$ is assumed to be analytic in $|\zeta| \leqslant 1$ and is such that $z_\zeta \neq 0$ there, at least for some period of time. We denote the Taylor's expansion of $h(\zeta, t)$ by $h(\zeta, t) = a_1 \zeta + a_2 \zeta^2 + \cdots$, where the constant coefficient has been set to zero—this is equivalent to a specific choice of origin for ζ.

A set of evolution equations for the coefficients $a_0, a_1, \ldots$ is obtained in Wang and Suo (1997) by consideration of the free energy variation δG associated with an arbitrarily small change in the pore shape. This leads to a system of equations of the form $\sum_k H_{ik} \dot{a}_k = f_i$ where $f_i = -\partial G / \partial a_i$ are generalized forces and where the entries of the matrix H_{ik} depend on a_i and v, which in turn is defined by $\zeta = e^{iv}$. Here we present a more compact representation for the map z, generalized to include the regularization term, which is rather simply derived by application of the Poisson integral formula. Spectral methods based on this formulation are easy to construct, and consequently are useful in the verification of the more complicated method described in Section 3.2.1.

To begin, note that the outward unit normal to the void surface can be written $N = iz_s$, where the subscript denotes differentiation with respect to s, the arclength traversed in the clockwise direction. Substitution of the relation $V_n = Re\{z_t \bar{N}\}$ into Eq. (13) yields, after a bit of algebra

$$Re\left\{\frac{z_t}{\zeta z_\zeta}\right\} = R(\zeta, t), \tag{17}$$

which holds on $|\zeta| = 1$; here

$$R(\zeta, t) = \frac{\zeta}{|z_\zeta|^2} \frac{\partial}{\partial \zeta} \frac{\zeta}{|z_\zeta|} \frac{\partial}{\partial \zeta} \left[(\gamma + \gamma'')\kappa - \frac{c\kappa^3}{2} + c \frac{\zeta}{|z_\zeta|} \frac{\partial}{\partial \zeta} \frac{\zeta}{|z_\zeta|} \frac{\partial}{\partial \zeta} \kappa - \Lambda\omega \right]. \tag{18}$$

In deriving the above we have used the identity $z_s = i\zeta z_\zeta / |z_\zeta|$ on $|\zeta| = 1$. The curvature $\kappa(\zeta, t)$ and surface energy density γ are determined from the map $z(\zeta, t)$ using the relations $\kappa = -(1/|z_\zeta|)Re(1 + (\zeta z_{\zeta\zeta}/z_\zeta))$ and $\cos 4(\theta - \theta_0) = Re\{(\zeta z_\zeta / |z_\zeta|)^4 e^{-4i\theta_0}\}$. Note that the quantity within braces in (17) is an analytic function of ζ for $|\zeta| \leqslant 1$. From the Poisson integral formula (Mikhlin, 1957), it follows that for $|\zeta| < 1$

$$z_t = \zeta z_\zeta [I(\zeta, t) + iQ], \tag{19}$$

where Q is a real constant and

$$I(\zeta, t) = \frac{1}{2\pi i} \oint_{|\zeta'|=1} \frac{d\zeta'}{\zeta'} \left[\frac{\zeta' + \zeta}{\zeta' - \zeta} \right] R(\zeta', t).$$

Examination of (19) as $\zeta \to 0$ indicates that $Q = 0$.

Eq. (19) is extended to the unit circle $\zeta = e^{iv}$ by deforming the contour in the usual way. This results in a principal value integral and contribution from a residue, i.e.,

$$z_t = -(\mathscr{H}[R](v,t) + iR(v,t))z_v, \qquad (20)$$

where $R(v,t)$ is given by (18) after the substitution $\zeta = e^{iv}$ and the operator $\mathscr{H}$ is the Hilbert transform, defined by

$$\mathscr{H}[F](v,t) = \frac{1}{2\pi} PV \int_0^{2\pi} F(v',t) \cot \frac{(v'-v)}{2} \, dv'.$$

The singular integral is defined in the Cauchy principal value sense. Eq. (20) gives the final form for the time evolution of the map. It is coupled to the elasticity through the strain energy density term ω in (18).

The elastic stresses for a given interfacial shape $z(\zeta, t)$ may be determined by employing well known techniques in the complex variable formulation of two-dimensional elasticity (Muskhelishvili, 1953). The elasticity problem is first restated in terms of the Goursat functions $f(z)$ and $g(z)$, which are defined to be analytic functions in the material region $z \in D$, for $z = x + iy$. The stresses are determined in terms of the Goursat functions as

$$\sigma_{11} + \sigma_{22} = 4 \, Re\{f'(z)\}, \qquad (21)$$

$$\sigma_{22} - \sigma_{11} + \sigma_{12} = 2[\bar{z}f''(z) + g''(z)]. \qquad (22)$$

An expression relating the displacements to f and g can also be determined, although it is not necessary for our purposes (in the following we need only ensure that displacements are single valued). The functions $f(z)$ and $g(z)$ must also satisfy appropriate boundary conditions as stated below.

First consider the boundary conditions at infinity. From (21) and recalling that stresses are non-dimensionalized by σ_1 it follows that

$$f(z) \sim \frac{1 + \chi + iC_1(t)}{4} z + C_2(t) + O\left(\frac{1}{z}\right) \quad \text{as } |z| \to \infty,$$

where $C_1(t)$ is a real and $C_2(t)$ a complex constant to be specified later. The behavior of $g'(z)$ at infinity is determined from (22), with the result

$$g'(z) = \frac{\chi - 1}{2} z + C_3(t) + O\left(\frac{1}{z}\right) \quad \text{as } |z| \to \infty, \qquad (23)$$

where $C_3(t)$ is a complex constant. The possible presence of $\ln z$ terms in (23) arising from the integration of $g''(z)$ is ruled out by the requirement of single-valued displacements. The remaining boundary condition is the zero traction condition (5), which is written in terms of the mapping variable ζ as (Muskhelishvili, 1957)

$$f(\zeta) + z(\zeta) \frac{\overline{f'(\zeta)}}{\overline{z'(\zeta)}} + \frac{\overline{g'(\zeta)}}{\overline{z'(\zeta)}} = C_4(t), \qquad (24)$$

where $|\zeta| = 1$ and $C_4(t)$ is a constant. The latter may be arbitrarily prescribed on a simply connected component of the boundary and thus we set $C_4(t) = 0$. Note that the choice of constants $C_1(t) - C_3(t)$ does not affect the stresses; for convenience C_1 and C_3 are set to zero, with C_2 then determined from (24) (see Muskhelishvili, 1957).

Eq. (24) is employed to derive an integral equation for f after the elimination of g by projection onto an appropriate function space. For a function $F(\zeta, t)$ with Laurent series expansion $F = \sum_{k=-\infty}^{k=\infty} c_k \zeta^k$ we denote by $F_+ = \sum_{k=1}^{k=\infty} c_k \zeta^k$ the projection onto positive powers of ζ, $F_- = \sum_{k=-\infty}^{k=-1} c_k \zeta^k$ is the projection onto negative powers, and $F_0 = c_0$ is the projection onto the constant component. In terms of these projections, the operator $\mathcal{H}$ has the form (Mikhlin, 1957)

$$\mathcal{H}[F] = i(F_+ - F_-) \tag{25}$$

from which it follows that $\frac{1}{2}(-i\mathcal{H}[F] + F) = F_+ + F_0/2$. Note also that $\overline{g'(\zeta)}/\overline{z'(\zeta)} = ((\chi - 1)/2)a_0\zeta + O(1/\zeta)$ so that application of the '+' operator to Eq. (24) yields the desired integral equation for f

$$f + z(\zeta)\frac{\overline{f'(\zeta)}}{\overline{z'(\zeta)}} - i\mathcal{H}\left[f + z(\zeta)\frac{\overline{f'(\zeta)}}{\overline{z'(\zeta)}}\right] = -(\chi - 1)a_0\zeta \tag{26}$$

where we have utilized the comment following (25) to write the projection in a simple form using the Hilbert transform.[2] The strain energy density is computed from f using (15) and (21), giving

$$\omega(\zeta, t) = 4\left[Re\,\frac{f_\zeta}{z_\zeta}\right]^2. \tag{27}$$

In summary, the system of Eqs. (20) and (26) with ω determined from (27) make up the conformal map formulation of our problem.

3.1.1. Numerical method for conformal map formulation

The system of Eqs. (20), (26) are in a particularly convenient form for numerical computation. Given the solution $z_j^n = z(v_j, t^n)$ and $f_j^n = f(v_j, t^n)$ at N node points and at time t^n, the right-hand side of the map evolution equation (20) is evaluated in $O(N \ln N)$ operations by using the Fast Fourier Transform (FFT) via relation (25). Derivatives are computed using the FFT in the usual way. It is then straightforward to update the map to time t^{n+1}. Once the update of z is obtained, the integral equation (26) is solved to obtain f at time t^{n+1}. This can be done directly, i.e., by writing as a linear system and inverting, or by employing an iterative technique such as the Generalized Minimum Residual algorithm (GMRES) (Saad and Schultz, 1986). (A method involving the direct application of (24) to form a linear system of equations for the coefficients in a truncated Laurent series for f is given in Muskhelishvili (1957) and implemented numerically in Wang and Suo (1997).) We have tried each of the above methods with comparable results, although the iterative technique has a speed advantage, since the linear operator in (26) can be applied to an iterate $f^{(j)}$ in only $O(N \ln N)$ operations.

Unfortunately, explicit methods for updating (20) suffer from severe time step constraints due to the presence of high-order terms. These constraints are alleviated by employing a simple semi-implicit method as described in Press et al. (1992), at the

---

[2] The Fredholm alternative is satisfied by enforcing a requirement that the coefficient of the $1/\zeta$ term in the Laurent series for f is real.

expense of having to do a single matrix inversion per time step. The inversion is implemented here using Gaussian elimination involving $O(N^3)$ operations, although this could be improved to $O(N^2)$ by employing iterative techniques. The algorithm as implemented is spectrally accurate in space and first order in time, which was sufficient for our purposes.

The conformal map formulation is also useful for the computation of non-linear steady states. Setting $V_n = 0$ in (13) and integrating twice with respect to arclength, we find that the steady states satisfy

$$(\gamma + \gamma'')\kappa - \frac{c\kappa^3}{2} - c \frac{1}{|z_v|} \frac{\partial}{\partial v} \frac{1}{|z_v|} \frac{\partial}{\partial v} \kappa - \Lambda\omega = K_1, \tag{28}$$

where, since we are looking for solutions periodic in arclength s, the term $K_2 s(v)$ that would appear on the right-hand side is set to zero. The constant K_1 is an unknown.

In general there are N unknowns associated with the real and imaginary parts of a_j for $j = 0, \ldots, N/2 - 1$, plus one unknown corresponding to the constant K_1. The $N + 1$ equations to be solved are (28) at the N independent nodes, and the conservation of mass equation fixing the area of the void at π. The non-linear equations are solved using a Newton iteration; at each iterate the elasticity and hence ω is updated by solving (26) in the fashion described above. It is noted that the number of unknowns may be reduced to $N/4 + 2$ by making use of the bilateral symmetry of the void. Initially we employ Λ as a bifurcation parameter, beginning the iterations at $\Lambda = 0$ with an approximate steady solution from the time dependent code for a given value of ε and c. The iterations are restarted after incrementing Λ using the converged solution at the previous value. At a turning point we change parameters, using a_0 as a bifurcation parameter and incorporating Λ as an unknown.

3.2. Arclength–angle formulation

The numerical method based on the conformal map formulation incurs difficulties when computing the long time evolution for positive regularization $c > 0$. The cause is a fingering instability for which the emerging fingers are poorly resolved. This is due to inadequate point spacing on the physical interface z for equally spaced points on the unit disk in the ζ plane—a common problem for conformal map parameterizations in cases involving fingering type behavior (Siegel et al., 1996; Ceniceros and Hou, 2000). Rather than adopt nonuniform spacing or local remeshing, we overcome this difficulty by reformulating the problem in terms of arclength and angle variables. This formulation provides more uniform point spacing on the physical interface, and has an important added benefit. Specifically, since the highest derivative term coming from the regularization appears linearly in θ with a constant coefficient, implicit time integration methods may be efficiently implemented (i.e., involving only the inversion of a diagonal matrix at each time step). The advantages of using the arclength–angle formulation in other problems are discussed in Kessler et al. (1987), Hou et al. (1994), Jou et al. (1997), and Akaiwa et al. (2001).

The interface is parameterized in terms of an equal arclength variable $\alpha \in [0, 2\pi]$. More precisely, α has the property that if s measures arclength along the interface,

then $s_\alpha(\alpha, t)$ is independent of α, and depends only on time. The dependent variables in the scheme are $\theta(\alpha, t)$ and s_α, rather than the x and y positions. For any evolving two-dimensional curve with normal velocity $V_n(\alpha, t)$ and tangential velocity $T(\alpha, t)$, these variables satisfy the system of equations (Gurtin, 1993; Hou et al., 1994)

$$\theta_t = \frac{V_{n_\alpha}}{s_\alpha} + \frac{T\theta_\alpha}{s_\alpha}, \tag{29}$$

$$s_{\alpha t} = T_\alpha - V_n \theta_\alpha, \tag{30}$$

where in our application an expression for V_n is given by (13), with $\kappa = -\theta_\alpha/s_\alpha$. Note that there is some arbitrariness in the assignment of $T(\alpha, t)$; here this term is chosen so that the right-hand side of (30) is independent of α. This leads to (see Hou et al., 1994)

$$\dot{A}(t) \equiv s_{\alpha t} = -\frac{1}{2\pi} \int_0^{2\pi} V_n \theta_\alpha \, d\alpha, \tag{31}$$

$$T(\alpha, t) = \frac{1}{2\pi} \int_0^\alpha V\theta_\alpha \, d\alpha - \frac{\alpha}{2\pi} \int_0^{2\pi} \theta_\alpha \, d\alpha, \tag{32}$$

where for convenience $T(0, t)$ has been set to zero and the notation $A(t) = s_\alpha$ has been introduced. The key attribute of this formulation is that the highest order term in the equation of motion for θ (coming from the third term on the right-hand side of (13)) appears linearly with constant coefficients. This fact is exploited in the construction of an efficient numerical method, i.e., one that has no time step constraint associated with the regularization term yet is explicit in Fourier space.

We also need to solve the elasticity problem to obtain the stresses on the boundary. The method of reduction of the elasticity problem to an integral equation that was used in Section 3.1 is not applicable here, since it relies on knowledge of the conformal map which is now not available. Instead, we employ a method based on Cauchy integrals. It is first convenient to define the function $\phi(z)$ by

$$\phi(z) = f(z) - \frac{1+\chi}{4} z, \tag{33}$$

i.e. where the unbounded component of f at infinity is removed. Denote the void boundary by $z(\alpha)$, and write $\phi(\alpha) = \phi(z(\alpha))$. An integral equation for $\phi(\alpha)$ is obtained by adapting the derivation for elastic particles (Mikhlin, 1957; Muskhelishvili, 1957) to the case of holes in an infinite solid. The equation takes the form

$$\frac{\phi(\alpha)}{2} - 2 Re \left[\frac{1}{2\pi i} \int_0^{2\pi} \frac{\phi(\alpha') z_\alpha(\alpha')}{z(\alpha') - z(\alpha)} \, d\alpha' \right] + \int_0^{2\pi} \frac{\bar{\phi}(\alpha') \bar{z}_\alpha(\alpha')}{z(\alpha') - z(\alpha)} \, d\alpha'$$

$$- \frac{1}{2\pi i} \int_0^{2\pi} \phi(\alpha') \frac{d}{d\alpha'} \frac{z(\alpha') - z(\alpha)}{\bar{z}(\alpha') - \bar{z}(\alpha)} \, d\alpha' = -\frac{1}{2} F(\alpha) + \frac{1}{2\pi i} \int_0^{2\pi} \frac{F(\alpha')}{z(\alpha') - z(\alpha)} \, d\alpha',$$

where $F(\alpha) = (1 - \chi) z(\alpha)/2 - (1 + \chi)\overline{z(\alpha)}/2$ and the dependence on t has been suppressed. All integrals with singular kernels are in the Cauchy principal value sense. From knowledge of ϕ the stress function f is recovered from (33), and the strain energy density ω follows from the relation $\omega = 4[Re\, f'(z)]^2$. An alternative approach

to obtain ϕ, based on the so-called Shermann–Lauricella formulation, is presented in Greengard et al. (1996). We have implemented numerical schemes based on both approaches and find no difference in terms of numerical efficiency or accuracy.

3.2.1. Numerical scheme based on arclength–angle formulation

The method is conveniently expressed in terms of the Fourier expansion $\theta(\alpha,t) = \sum_{k=-N/2}^{N/2-1} \hat{\theta}_k(t) e^{ik\alpha}$. The Fourier transform of (29) gives an equation for $\hat{\theta}_k(t)$ which is written in the form

$$\frac{\mathrm{d}\hat{\theta}_k}{\mathrm{d}t} = -\frac{ck^6}{A^6}\hat{\theta}_k + \hat{N}_k(\alpha,t). \tag{34}$$

The second term above is the Fourier coefficient of the highest order contribution which is dominant at small scales; the third term refers to the Fourier coefficient of the portion $N(\alpha,t)$ that remains after extracting the highest order term. In particular,

$$N(\alpha,t) = \frac{1}{A^3}\frac{\partial^3}{\partial\alpha^3}\left[-(1-15\varepsilon\cos\theta)\frac{\theta_\alpha}{A} + \frac{c\theta_\alpha^3}{2A^3} - \Lambda\omega\right] + \frac{T\theta_\alpha}{A}.$$

The system of Eq. (34) is combined with the ODE for A in (31). The location of the interface is recovered from knowledge of $\theta(\alpha,t)$ and $A(t)$ by integrating $(x_\alpha, y_\alpha) = A(\cos\theta, \sin\theta)$.

An implicit time integration method can be applied to system (31), (34) in a straightforward manner. We experimented with a number of time discretization methods; a mixed implicit/explicit method was found give a desirable measure of control over relative degree of smoothing (which provides stability) versus level of accuracy. The scheme is given by

$$\frac{\hat{\theta}_k^{n+1} - \hat{\theta}_k^n}{\Delta t} = -ck^6\left[\eta\frac{\hat{\theta}_k^{n+1}}{(A^6)^{n+1}} + (1-\eta)\frac{\hat{\theta}_k^n}{(A^6)^n}\right] + \Delta t\hat{N}_k^n \tag{35}$$

from which an explicit formula for $\hat{\theta}_k^{n+1}$ follows. Here the superscript n denotes evaluation at time t^n. The differential equation for A is discretized with an explicit method and updated before θ, so that A^{n+1} can be used in the θ discretization. It is useful to define the amplification factor $\alpha_m(k) = |(1 - \Delta t ck^6(1-\eta)(A^n)^{-6})/(1 + \Delta t ck^6\eta(A^{n+1})^{-6})|$; from this definition and (35) it follows that a discrete mode of wavenumber k grows like $[\alpha_m(k)]^n$ upon neglecting the lower order terms $N(\alpha,t)$. The adjustable parameter $\eta \in [0,1]$ sets the degree of smoothing; $\eta = 0$ corresponds to a standard first-order forward Euler scheme and $\eta = 1/2$ to second order Crank–Nicholson, whereas $\eta = 1$ corresponds to fully implicit backwards Euler. The integration scheme is most stable for $\eta = 1$, in which case the amplification factor α_m decreases linearly with k, while the most accuracy but least amount of smoothing occurs for $\eta = 0.5$, so that $\alpha_m \to 1$ as $k \to \infty$. For most of the calculations reported in this paper η is set at 0.6.

Other details of the method are as follows. Derivatives are computed using the FFT, singular integrals are evaluated using alternate point trapezoidal rule (Sidi and Israeli, 1988) and other integrals by trapezoidal rule, so that all spatial discretizations are spectrally accurate. Spectral filtering (Krasny, 1986) is applied to suppress the spurious growth of short-wavelength modes generated by round-off error. In some cases

an aliasing filter as described in Hou et al. (1994) was found to prevent the premature onset of aliasing instabilities.

The present method was checked against the conformal map method (which was independently validated as described below) and found to give identical results. During simulations the number of modes is doubled and the time step decreased until there are no detectable differences in the solution within plotting accuracy, nor any significant changes in other quantities of interest.

The arclength–angle formulation may also be used to compute steady-state solutions. The variable A is used as the bifurcation parameter, since this is expected to be monotonically increasing along the response curve. In general there are $N + 1$ unknowns for N discretization points, corresponding to $\theta(\alpha_1), \ldots, \theta(\alpha_N)$ and Λ. The number of unknowns is reduced to $N/4$ by employing the reflection symmetry in the x- and y-axis. Eq. (30) then provides $N/4 - 1$ equations for the unknowns, one for each grid point in the interior of the first quadrant. The constraint of fixed area provides the final equation. This method is used to find highly deformed steady shapes lying on the upper branch of the response curves for $c > 0$. Otherwise, the conformal map method is more accurate for a given number of discretization points, since the map tends to cluster points near regions of high curvature.

3.3. Validation

Exact equilibrium solutions (Burton et al., 1951; Mullins, 1962) for $\varepsilon > 0$ and $c = 0$ are used as a check on the numerical computation in the absence of elasticity. Equilibrium solutions computed using the time-dependent conformal map method (see Section 3.1.1) with $N = 128$ node points, starting from a circular initial profile, were found to be indistinguishable (to plotting resolution) from the exact solution for ε up to 0.065, just below the value for which corners are present on the steady interface and the initial value problem becomes ill-posed. It has also been verified that the exact solution is indeed an equilibrium profile for our steady-state algorithm (see Section 3.2.1).

As a check on our numerical method for solving the elasticity problem we computed the stress at the interface using fixed void shapes for which there exist exact analytical solutions (Muskhelishvili, 1957; Gao, 1995). One such class of shapes are ellipses, for which exact solutions are available for arbitrary χ. In the case of uniaxial tension $\chi = 0$, the stress function corresponding to the family of ellipses $z(\zeta) = 1/\zeta + m\zeta$ for real m is given by $f(\zeta) = [1/\zeta + (2 - m)\zeta]/4$. Exact solutions also exist in the case $\chi = 1$ for a family of curves known as hypocycloids, defined by $z = 1/\zeta + \delta\zeta^{n-1}/(n-1)$ for positive integer n, where δ parameterizes the family. For $\delta = 1.0$ the hypocycloid interface has four zero-angled cusps. The elasticity solution is given by $f(\zeta) = \frac{1}{2}((1/\zeta) - \delta/(n-1)\zeta^{n-1})$. For a given ellipse or hypocycloid profile, we verified that the numerically computed stress function coincided with the exact solution up to round-off error. (In the case of hypocycloids $n \leqslant N/2$ is required for this agreement, since the largest wavenumber mode that can be represented by N grid points is $e^{i(N/2-1)\nu}$.) The agreement up to round-off was verified even for cusped profiles with $\delta = 1.0$. The ability to compute the elastic stresses accurately in the neighborhood of a zero angled cusp is one advantage of the conformal map representation.

An additional check on the numerical accuracy is provided by conservation of void area. For the simulations reported in the next section the area is typically conserved to within 10^{-6}, falling to 10^{-3} for the very late stage evolution like that shown in Fig. 12. The reason for the decline can be attributed in part to the large number of derivatives (i.e., 6) on the highest order term, which leads to amplification of round-off error and a loss of accuracy in fixed precision calculations when N is large.

4. Numerical results

4.1. The well-posed case: $\varepsilon < 1/15$

We first consider results for the well-posed case, $\varepsilon < 1/15$. Results are reported for both zero regularization and small positive regularization; the latter case is used for comparison against the interfacial evolution when $\varepsilon > 1/15$ (Section 4.2), where regularization is required. The conformal map method is used for all results reported in this section, with the exception of transient calculations in the case $c > 0$.

4.1.1. $c = 0$
The steady solution branch is first calculated for isotropic surface energy $\varepsilon = 0$ starting from a circle at $\Lambda = 0$. The computed solution branch is represented in Fig. 1a by plotting the deformation D of the void versus Λ, where D is defined by

$$D = \frac{R_{\max} - R_{\min}}{R_{\max} + R_{\min}}.$$

Here $R_{\max}$ and $R_{\min}$ are the maximum and minimum distances from the origin to a point on the void surface. The interfacial shapes at representative locations indicated by '+' markers on the solution branch are presented in Fig. 1b. The main feature of the solution branch is the presence of a turning point at $\Lambda = \Lambda_c \sim 0.54$, which divides the response curve into a lower and upper branch. Our numerical simulations of the time-dependent evolution show that the lower branch corresponds to stable steady states, in that the evolution starting from a circular void eventually reaches a stationary profile on the lower branch. In contrast the upper branch is found to be unstable.

It is interesting to contrast the steady-state response curve with that for the stress driven instability on the surface of a semi-infinite solid as reported in Spencer and Meiron (1994). There, the problem is non-dimensionalized by defining a characteristic length $l = \gamma_0/\omega_0$ where γ_0 is the (isotropic) surface energy and $\omega_0 = \sigma_1^2(1 - \nu^2)/(2E)$ is a characteristic value of the strain energy density. Periodic steady solutions are then calculated using the wavelength of the periodic box as a bifurcation parameter. The formulation is essentially equivalent to ours if one associates the non-dimensional wavelength λ/l with the parameter Λ. Like the current study, there is a critical value λ_c/l of the bifurcation parameter above which steady states no longer exist. However, in contrast to Fig. 1a the solution branch is found to *terminate* at λ_c/l, with the termination point corresponding to a cusped profile. This difference is ascribed to geometry. More precisely, the steady solution along the upper branch in Fig. 1a is approaching
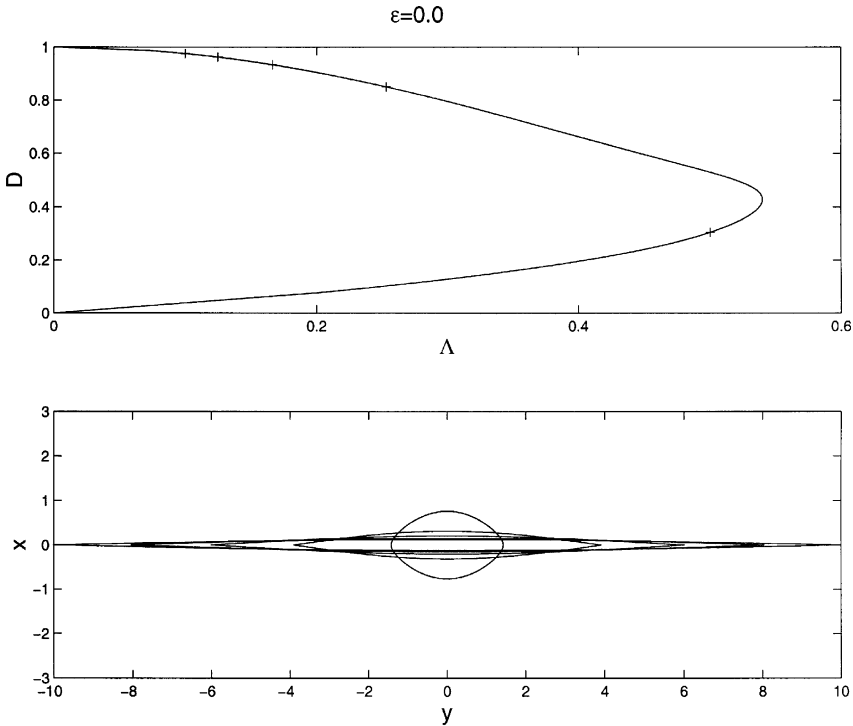
Fig. 1. (a) Steady-state response curve showing the deformation D versus Λ for zero anisotropy ($\varepsilon = 0$) and $c = 0$. The crosses ($+$) denote positions on the curve for which surface profiles are plotted in (b). (b) Steady-state interface shapes at locations on the response curve denoted by crosses in (a). The steady void becomes more elongated as one moves along the curve from the origin $(0,0)$ to the end at $(1,0)$. Note the figure has been rotated by $90°$.

an infinite vertical 'crack' with planar faces, which is an exact solution at $\Lambda = 0$. Geometrical constraints rule out such a solution in the semi-infinite solid.

The form of the solution branch in Fig. 1a suggests that there is no steady solution for $\Lambda > \Lambda_{\mathrm{c}}$.[3] Evidence from our numerical calculations shows that for supercritical Λ (i.e., $\Lambda > \Lambda_{\mathrm{c}}$) the void is driven to form transient cusps. Fig. 2 presents our evidence for transient cusp formation in the case $\Lambda = 1.0$. Fig. 2a shows a semilog plot of the tip radius R_{tip} versus time for an increasing collection of node points. The trend suggests convergence of the R_{tip} versus t curve as N is increased, and furthermore predicts that R_{tip} tends to 0 in finite time. The surface velocity near the emerging cusp tips becomes very large near the critical time (e.g., reaching $O(10^5)$ by $t = 6.53$ for $N = 256$), consistent with expectations that the tip velocity diverges at the critical time. A set of profiles for the simulation at $N = 256$ including one at the approximate critical

---

[3] Efforts to find other solution branches were not successful, although an exhaustive search was not undertaken.
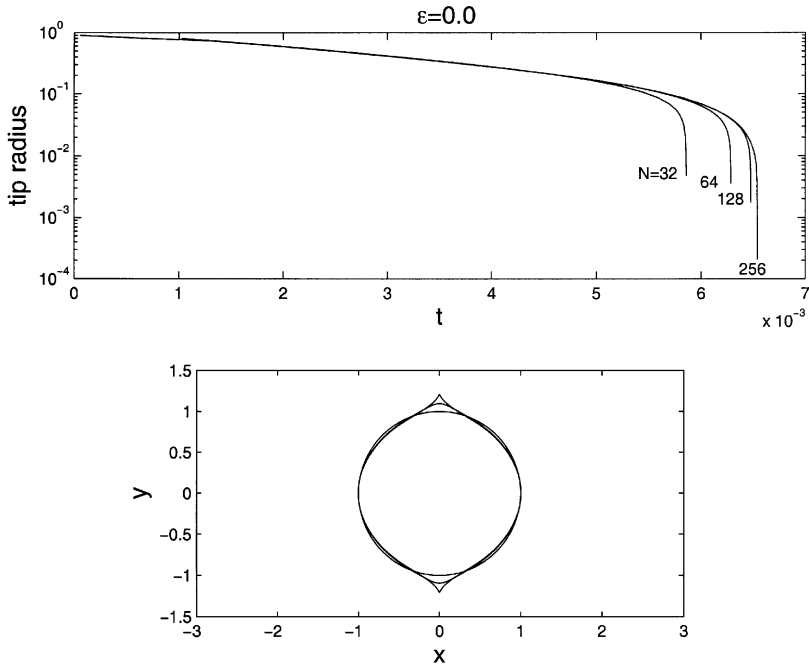
Fig. 2. (a) Plot of tip radius of curvature $R_{\text{tip}}(v = \pm\pi/2)$ versus time for an evolving void. Parameter values are $\varepsilon = 0.0$, $\Lambda = 1.0$, and $c = 0.0$. Curves are shown for $N = 32$, 64, 128 and 256 discretization points. (b) Void profiles for the numerically computed evolution. Parameter values are as in (a), and $N = 256$. The final (cusped) profile corresponds to the terminal point on the branch shown in (a).

time is shown in Fig. 2b. The void profile at the critical time (as well as the value of the time) differs from that in the study by Wang and Suo (1997); it is suggested that the number of nodes employed in that study (i.e., 16) is insufficient to resolve the interface. In contrast, the void shapes and critical time obtained in the finite element study Xia et al. (1997) very closely match those found here, although slightly different far-field conditions are employed. Interestingly, we find a critical value $\Lambda_c \sim 0.54$ for cusp formation is close to the value predicted by Suo and Wang (1994) using a simple model based on a purely elliptical void shape.

Similar results are obtained when $0 < \varepsilon < 1/15$. In particular the form of the computed steady solution branches is qualitatively the same as for $\varepsilon = 0$. Transient cusp formation is still observed for Λ large enough, although the time to cusping is reduced as Λ is increased (see also Wang and Suo, 1997). This is to be expected, since surface energy at the poles of the void is lower (for increased Λ) in the early stages of evolution.

4.1.2. $c > 0$

Our steady-state calculations for $\varepsilon < 1/15$ and $c > 0$ show that the form of the steady solution branch is qualitatively similar to that for $c = 0$. For given c, the branch exhibits
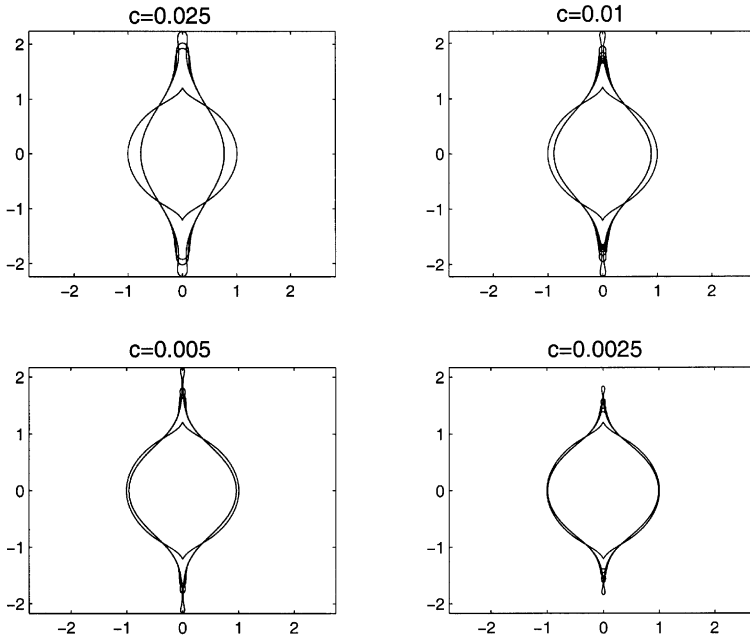
Fig. 3. Void evolution for a decreasing sequence of c in the isotropic case $\varepsilon = 0$, for $\Lambda = 1.0$. The times the final profiles are $t = 0.092$ ($c = 0.025$), 0.0456, 0.0273, and 0.0178 ($c = 0.0025$). Shown for comparison is the final cusped profile from Fig. 2b.

a turning point which again suggests there is no steady solution for Λ greater than a critical value $\Lambda_c(c)$ that depends on the regularization. However, calculations of the transient evolution do not show the development of cusps for supercritical Λ, but rather display a surprising filamenting instability. For example, the interfacial evolution at the supercritical value $\Lambda = 1.0$ is depicted for a decreasing sequence of c in Fig. 3. Also shown for comparison is the $c = 0$ cusped solution from Fig. 2b. The void is seen to emit slender high speed filaments which lengthen indefinitely as time progresses; this behavior is referred to as *tip streaming*. The tip streaming occurs for arbitrarily small c, as long as $\Lambda > \Lambda_c(c \to 0)$. Interestingly, away from the tip streaming filament the interfacial profile is increasingly more faithful to the $c = 0$ cusped solution as c is reduced; this is suggestive of convergence of the dynamics to the cusping solution as $c \to 0$. We discuss the significance of theses results in more detail in Section 4.2, when evolution for $\varepsilon > 1/15$ is considered.

4.2. The evolution for $\varepsilon > 1/15$

We now examine the steady-state solution branches and time-dependent evolution for $\varepsilon > 1/15$, for which regularization is required as the initial value problem is ill-posed in its absence. Attention is focused on ascertaining information concerning the limit $c \to 0$.

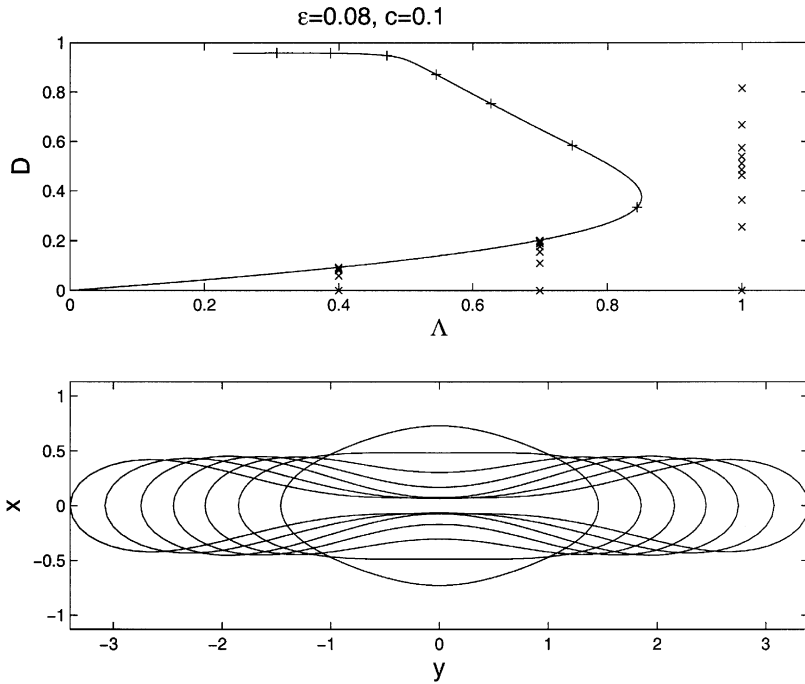Fig. 4. (a) Steady-state response curve plotting D versus Λ for $\varepsilon = 0.08 > 1/15$ and $c = 0.1$. The crosses ($+$) denote positions on the curve for which surface profiles are plotted in (b). The '$\times$' markers illustrate the deformation D in time-dependent simulations. The time intervals between markers is $\Delta t = 0.5$ for $\Lambda = 0.4$ and 0.7; for $\Lambda = 1.0$ the first three intervals are $\Delta t = 0.1$, the next five are $\Delta = 0.2$ and the final interval is $\Delta t = 0.078$ (b) Steady-state interface shapes at locations on the response curve denoted by crosses in (a). The void becomes more elongated as one moves along the curve starting from the origin $(0,0)$. Note the figure has been rotated by $90°$.

4.2.1. Nonlinear steady states

Fig. 4a shows the steady-state response curve for the representative case $c = 0.1$ and $\varepsilon = 0.08 > 1/15$. Like the $c = 0$, $\varepsilon = 0$ steady state, there is a turning point in the curve. This suggests that there is no steady solution for Λ greater than a critical value Λ_c. However, unlike the zero regularization case for $\varepsilon = 0$, we do not expect the evolution for $\Lambda > \Lambda_c$ to result in transient cusp formation. The behavior for $\Lambda > \Lambda_c$ is deferred until Section 4.2.2 where we consider transient evolution.

Steady-state shapes corresponding to the marked locations on the response curve are shown in Fig. 4b. The steady void profiles lengthen without limit as the upper branch is followed for decreasing Λ. Simulations of the transient evolution (for values of c down to 0.0025) verify that the lower branch corresponds to stable steady states. In contrast, the solutions represented by the upper branch are unstable.

An interesting question is whether steady solutions for all Λ are recovered in the limit $c \to 0$. This would be the case if for example $\Lambda_c \to \infty$ as $c \to 0$. However, Fig. 5 shows that the critical value Λ_c actually decreases as c is lowered. The figure indicates
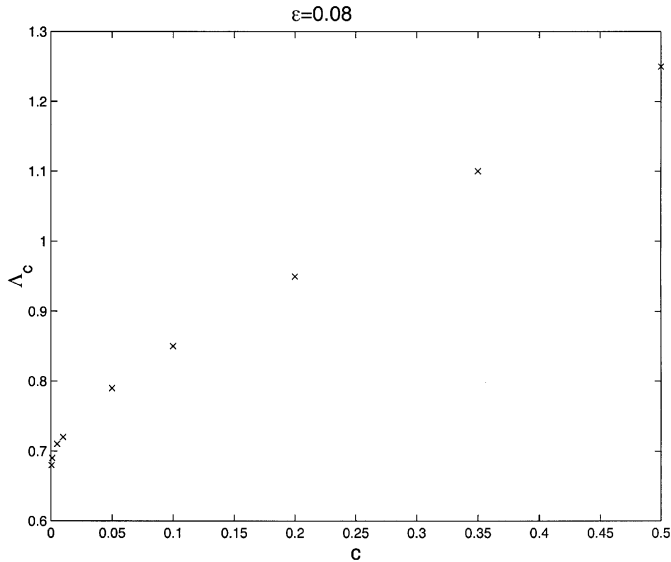
Fig. 5. Location of the turning point Λ_c versus regularization c, for fixed $\varepsilon = 0.08$. The value of Λ_c decreases as c is reduced.

that Λ_c approaches a finite non-zero value near 0.68 as $c \to 0$. Due to the large slope near $c = 0$ we cannot rule out the possibility that $\Lambda_c \to 0$ as $c \to 0$. However, one might argue that this is not likely since the existence of steady states for $\Lambda = 0$ leads us to expect that they exist for small positive Λ. Regardless, the important feature is that our computations imply that steady solutions (at least on this particular branch) no longer exist when $\Lambda > \Lambda_c(c \to 0)$ and c is sufficiently small.

One of our main interests is in the nature of steady solutions as the regularization c tends to zero. Figs. 6 and 7a depict the steady interfacial profiles for a decreasing sequence of c and fixed anisotropy ε in the absence of elasticity (Fig. 6) and with subcritical elasticity (Fig. 7a). These solutions are computed using continuation in c, for fixed ε and Λ. Fig. 6 shows that the expected behavior is realized in the absence of elasticity. More precisely, for small regularization the void shape resembles that of the exact zero regularization solution, but with rounded corners. As the regularization is further reduced the interface uniformly approaches the $c = 0$ shape. The trend suggests that in this case the $c \to 0$ steady solution equals the $c = 0$ exact solution, with admissible corners (Spencer, 2003, provides analytical justification for this behavior). The presence of corners in the limit $c \to 0$ avoids 'unstable' orientations i.e., those which are ill-posed in the zero regularization evolution.

When Λ is positive the trend likewise suggests that the interface develops corner-like regions as the regularization is reduced, suggesting the formation of true corners in the zero regularization limit. For example, Fig. 7a shows a sequence of steady-state profiles for decreasing c, one set of three curves each for the values $\Lambda = 0.3$ and 0.6. However, now there is no clear indication that the angles of the emerging corners will necessarily
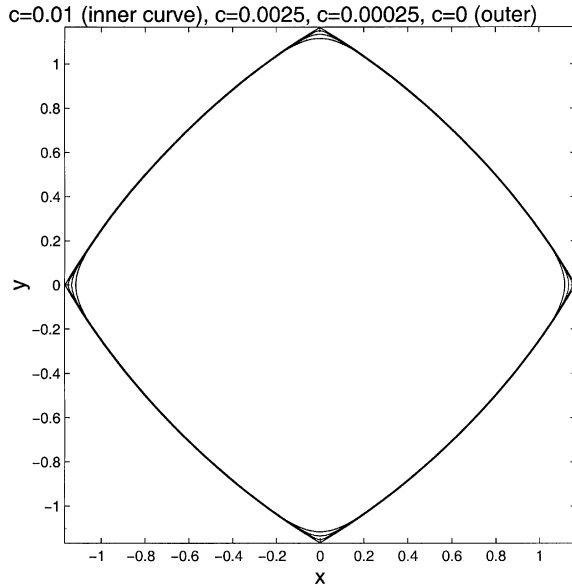
Fig. 6. Steady-state void shapes for $\varepsilon = 0.15$ and $\Lambda = 0$, at different levels of regularization. Curves are shown for $c = 0.01$ (innermost curve), 0.0025, 0.00025 and 0.0 (outermost curve). The profiles approach the zero regularization solution as c is reduced. It is noted that the four curves have the same area; the slight increase in area at the corners as c is reduced is compensated by a decrease in area along the edges.

correspond to that predicted by local equilibrium. Indeed, the trends indicate that the emerging corner angles at the uppermost and lowermost positions on the void surface are different than that of the local equilibrium solution, as depicted by the $\Lambda = 0$ curve. The lack of agreement between the predicted local equilibrium angle and that approached in the regularized problem is enhanced as Λ is increased, as is illustrated in the figure. As a further illustration, in Fig. 7b we plot normal angle θ versus arclength s for the profiles at $\Lambda = 0.6$ and 0 shown in Fig. 7a. The figure provides strong evidence of a jump in θ in the limit $c \to 0$ which is different from the jump in θ for the local equilibrium solution. In contrast, the emerging angles at the two side corners do appear to correspond to that predicted by local equilibrium.

We interpret the above results as follows. At any given fixed value of c, the regularized steady interface is smooth. Following Gurtin (1993) and Gurtin and Voorhees (1998) the force balance on smooth portions of the interface may be written in terms of 'configurational forces' and a generalized capillary force $\mathbf{C}$, defined by $\mathbf{C} = \gamma(\theta)\mathbf{t} + \gamma'(\theta)\mathbf{n}$ (zero regularization is assumed). Balance of forces on smooth portions of the interface is trivially satisfied. Force balance at a corner implies $\mathbf{C}(\theta_+) = \mathbf{C}(\theta_-)$, where $+$ and $-$ denote the right and left-hand limits to the corner. (The admissible angles are derived from the latter balance.) Therefore, even though each regularized interfacial profile satisfies the force balance at all points, the profile defined in the limit $c \to 0$ may not. This behavior may be surprising, yet cannot be ruled out in view of the potentially singular nature of the zero regularization limit. It is noted that numerical
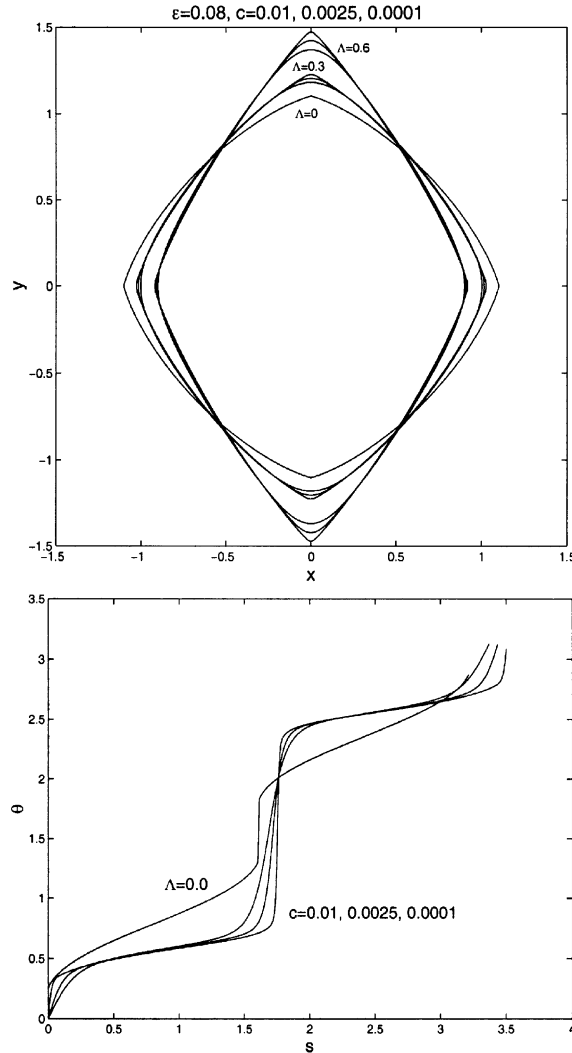
Fig. 7. (a) Comparison of steady shapes for $\Lambda = 0.3$ and 0.6, for a decreasing sequence of c. Here $\varepsilon = 0.08$. Curves are shown for $c = 0.01$ (innermost of a set of three curves at $\Lambda = 0.3$ or 0.6), $c = 0.0025$ and 0.0001 (outermost curve). Also shown for comparison is the $\Lambda = 0$ solution exhibiting local equilibrium corner angles. (b) Plot of θ versus arclength s for the solutions at $\Lambda = 0.6$ in (a); for reference the $\Lambda = 0$ plot is included. The regularization values are (left to right at jump) $c = 0.01$, 0.0025, and 0.0001. The curves are different lengths owing to the different total arclengths of the steady voids.

considerations limit the extent to which c may be reduced. Of course, it may be that for still smaller values of c than have been considered here the local equilibrium result will be approached in a small neighborhood of the corner.

At a true interfacial cusp or corner the elastic energy density diverges. However, the contribution to the total energy in a small neighborhood of the corner from the
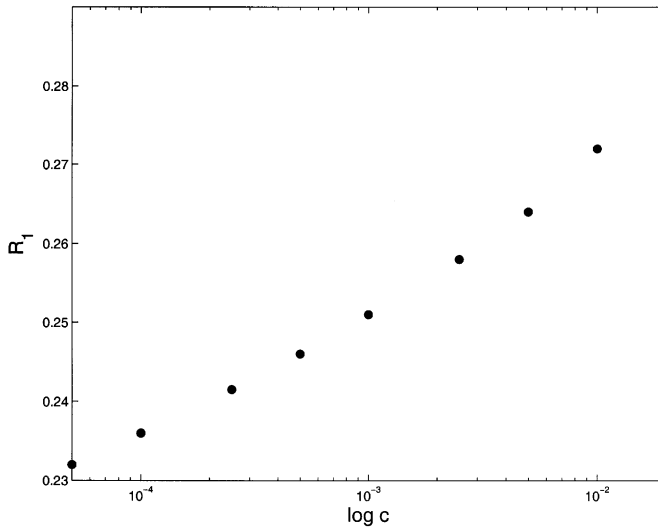
Fig. 8. Semi-log plot of ratio of third ('elastic energy') term in (13) to the first ('interfacial energy') term, versus regularization c.

(volumetric) elastic field is asymptotically smaller than that due to (interfacial) surface energy. This is the basis of arguments (Gurtin and Voorhees, 1998; Srolovitz and Davis, 2001) that elastic effects cannot modify the local equilibrium angle of a sharp corner. Such considerations do not preclude stress effects from influencing a corner angle in the zero regularization limit, since the regularization may act as a singular perturbation. However, these arguments do motivate us to consider the dominant balance between terms in Eq. (13) for steady-state voids in the limit as $c \to 0$, at an emerging corner. Specifically, we evaluate the ratio R_1 of the third term on the right-hand side of (13) (referred to as the 'elastic energy' term) to first ('interfacial energy') term; this ratio is plotted on a semi-log scale in Fig. 8. The ratio is evaluated at $\theta = \pi/2$, corresponding to the emerging upper corner, and for parameter values $\varepsilon = 0.08$ and $\Lambda = 0.6$. The figure shows that the relative magnitude of the elasticity term is slowly diminishing when compared with the surface energy term as c is reduced. Since the terms comprising (13) sum to zero for steady-state voids, the ratio of the second ('regularization') term to first ('interfacial energy') term approaches one.

We have fitted a line to the data in Fig. 8 (R_1 versus $\ln c$), with the best fit given by $R_1 = 0.309 + 0.008 \ln c$. This equals zero for $c \sim 10^{-17}$, which is consistent with the notion that the dominant balance in Eq. (13) at an emerging corner (for $c \to 0$ steady state voids) is between surface energy and regularization terms. The results of Fig. 8 are therefore suggestive of an 'inner region' where the surface energy term and the regularization term balance at leading order in c, with the elasticity contribution occurring at higher order. We surmise that the effect of elasticity on the emerging corner angle then comes from matching to an 'outer' solution for which the elasticity contributes to leading order. It must be cautioned, however, that the data are
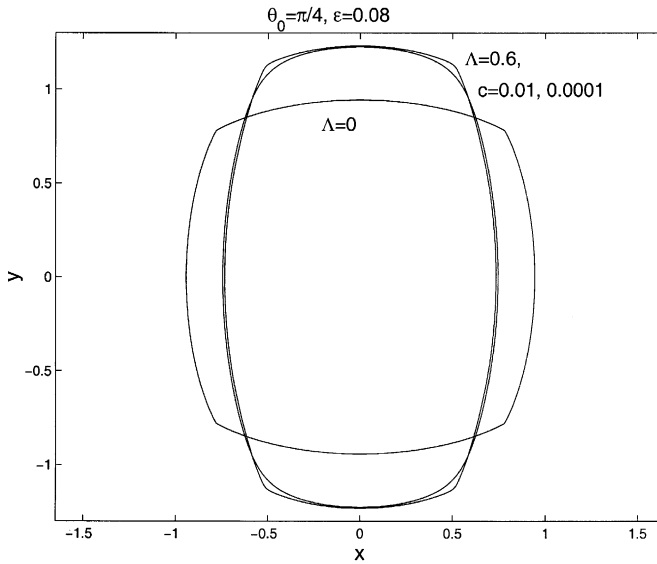
Fig. 9. Steady shapes for $\theta_0 = \pi/4$. Parameter values are $\Lambda = 0.6$, $\varepsilon = 0.08$, $c = 0.01$ (more rounded profile at corners) and $c = 0.0001$ (sharper corners). Included for comparison is the $\Lambda = 0$ solution exhibiting the local equilibrium angle at corners.

also consistent with a small but finite relative contribution from the elastic energy term as $c \to 0$, so a conclusive interpretation of our data awaits further analytical investigation.

Finally, we consider the effects on the steady void shape of changing the angle of maximum surface energy, θ_0 (see Eq. (2)). Fig. 9 depicts the steady shapes corresponding to $\theta_0 = \pi/4$, with the other parameters being the same as in Fig. 7a. Interestingly, the corner angles appearing as c is reduced seem to coincide with the local equilibrium angles. Effectively, as Λ is increased from zero the void is able to create new surface 'area' transverse to the applied stress (thereby reducing total elastic energy) simply by altering its aspect ratio, all the while preserving the $\Lambda = 0$ equilibrium angles, i.e., the admissible angles. However, this appears to be a special case. More precisely, for other θ_0 we observe that the deformation induced by increased elasticity is accompanied by alterations in the $c \to 0$ orientations, leading to non-admissible angles.

4.2.2. Transient dynamics for $c > 0$

The time-dependent behavior of the interface for $\varepsilon > 1/15$ is first considered in the representative case $c = 0.1$. We use a circular void as the initial shape for all transient calculations. Consulting Fig. 4a, it is observed that for subcritical Λ the transient solution locks onto a steady-state solution on the lower branch of the response curve. This is depicted by the '×' markers which give the deformation of the void at equally spaced time intervals. A more pressing question concerns the dynamics for $\Lambda > \Lambda_c$. In this case we have been unable to find a steady solution; the transient evolution depicted
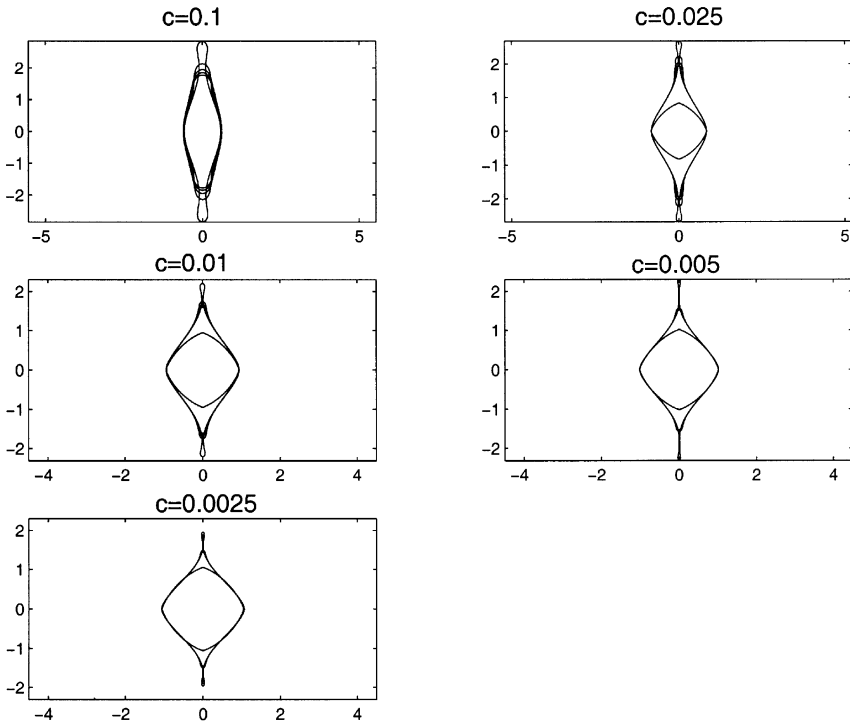
Fig. 10. Comparison of void evolution for a decreasing sequence of c, indicating 'tip-streaming' behavior. Parameter values are $\Lambda = 1.0$ and $\varepsilon = 0.08$. Also shown for comparison is the $\Lambda = 0$, $\varepsilon = 0.08$ steady solution (innermost profile in all but the $c = 0.1$ plot). This steady solution is scaled so that the diameter along the x-axis matches that of the time evolving void.

in Fig. 4a reflects the nonexistence of a steady limit by indicating that the deformation grows at an increasingly greater rate as time progresses.

The interfacial evolution at supercritical Λ is shown for a decreasing sequence of c in Fig. 10.

For comparison we have also included in all but the first plot the $\Lambda = 0$ steady solution depicting the local equilibrium corner angles. The plots indicate that at supercritical Λ the void eventually emits filaments (tip streaming), as was observed for $\varepsilon = 0$ in the case of positive regularization. It is noted that to accurately capture this behavior very small time steps are required—on the order of $\Delta t = 1 \times 10^{-7}$. The number of nodes required to resolve the *onset* of the phenomenon increases as c is lowered, e.g., $N = 1024$ for $c = 0.005$ and $N = 2048$ for $c = 0.0025$.

Since the critical value Λ_c for tip streaming decreases as c is lowered (cf. Fig. 5), it follows that the tip-streaming will be observed for arbitrarily small c, as long as $\Lambda > \Lambda_c(c \to 0)$. Furthermore, reducing the regularization c causes the tip-streaming filament to occur at earlier times, as can be seen by noting that the times for the final profile in each subplot of Fig. 10 are given by $t = 0.4, 0.103, 0.0486, 0.028$ and 0.01628

as c ranges from 0.1 to 0.0025. Reducing c also causes the tip-streaming filament to be thinner at its onset. At the same time the main body of the pore remains essentially 'frozen' in time. These observations suggest that in the limit $c \to 0$ the width of the tip-streaming filament tends to zero and the time dependent dynamics converge (almost everywhere) to a fixed closed profile.

Interestingly, as c is reduced the frozen main body of the pore (i.e., away from the tip-streaming filament) is becoming more faithful to the $\Lambda = 0$ equilibrium profile, even though $\Lambda > 0$ in the simulations. This is perhaps surprising, although a possible explanation is as follows. The behavior observed in the numerical simulations is distinguished by two time scales. There is a fast time scale, apparently dominated by surface anisotropy, in which the interface quickly gets rid of ill-posed angles by forming (smoothed out) 'corners'. This makes it evolve very quickly into something resembling the Wulff shape, as seen in Fig. 10. [4] Over longer times the effect of elasticity becomes apparent, and the corners at the top and bottom of the void get stretched out, eventually leading to tip streaming.

The above observations may be roughly quantified by appealing to linear stability theory. Consider first unstable interface motion driven by anisotropy only (i.e., $\Lambda = 0$). The wavenumber k_m of the fastest growing disturbance to a locally flat profile is easily seen to be proportional to $c^{-1/2}$, with a maximum growth rate $\sigma_m(k_m) \sim c^{-2}$. This gives a time scale τ_a for motion due to anisotropy satisfying $\tau_a \sim c^2$. On the other hand, when the motion is driven by elasticity only (i.e., neglecting anisotropy) then $k_m \sim c^{-1/3}$ and $\sigma_m(k_m) \sim c^{-1}$. This gives a time scale for the influence of elasticity on a locally flat profile, $\tau_e \sim c$, which for small c is larger than the time scale τ_a. Our numerical simulations give results which are consistent with these time scales, even for large interfacial deformations. For example, consider the times of the final profile in each subplot of Fig. 10 or Fig. 3 as a measure of the time scale τ_e. These times scale roughly like c, consistent with the above argument. Conversely, simulations of the evolution for $\Lambda = 0$ show that the time for the development of significant wrinkling scales roughly like c^2.

As c is reduced the elasticity seems to affect a more and more localized region, i.e., the tip streaming filament is becoming thinner. This gives the impression of convergence to the Wulff shape. However, on the basis of the numerical results one could argue for convergence to other shapes, for example a cusped configuration, as $c \to 0$. Similarities between the interfacial evolution in the tip streaming region for the isotropic case (see Fig. 3), in which convergence to a cusped profile is expected in the zero regularization limit, and the evolution for $\varepsilon > 1/15$ (Fig. 10) provide some pictorial evidence for this latter assertion. Unfortunately, we are restricted as to how far the regularization may be reduced due to the ill-posedness of the $c = 0$ evolution; as the regularization is reduced the large number of fast growing modes places increasing demands on the numerical simulation. Some of the numerical issues involved in computing for small regularization, in cases where the underlying problem is ill-posed, are discussed in the context of fluid dynamics in Siegel et al. (1996) and Ceniceros and

---

[4] For relatively small c or large ε the interface wrinkles with multiple corners localized near regions where the initial orientations are ill-posed, cf. Fig. 14.
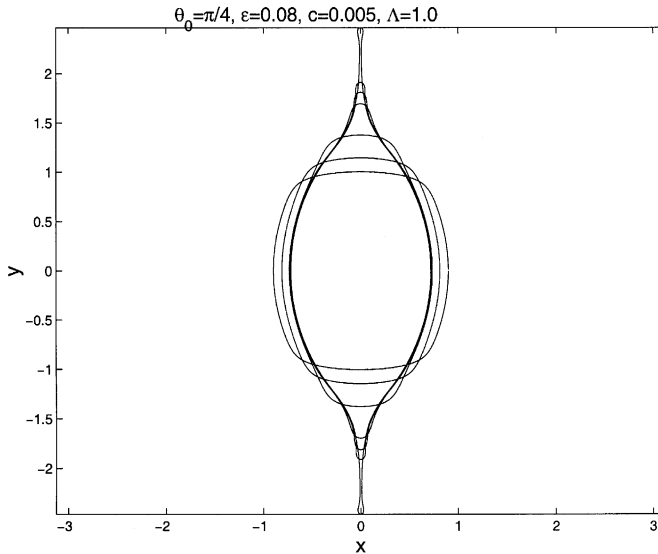
Fig. 11. Tip streaming of void for $\theta_0 = \pi/4$. Other parameter values are $\varepsilon = 0.08$, $c = 0.005$, and $\Lambda = 1.0$. The time increment between curves is 0.04 for the first two increments, 0.0102 for the third, 0.0003 for the fourth and 0.0001 for the final two increments.

Hou (2000). Future analytical investigation is therefore warranted to confirm the nature of the zero regularization limit.

It is interesting to also consider the interfacial evolution in the case when the angle of maximum surface energy is rotated. Fig. 11 presents numerical results for the case $\theta_0 = \pi/4$ and $c = 0.005$; the other parameter values are as in Fig. 10. At early stages in the evolution the profiles feature near corners with 'angles' that are similar to the local equilibrium angles. Eventually the two upper and lower corners begin to merge, at which point tip streaming occurs (note that immediately prior to tip streaming the interfacial shapes bear little evidence of the anisotropy). The indications then are that tip streaming is a generic feature of the evolution at large enough Λ.

To the best of our knowledge, tip-streaming of material surfaces evolving under surface diffusion has not been previously observed. We therefore further examine some of the features of this phenomenon during the long time evolution. Fig. 12 shows the development of the void during late stages in the evolution for $c = 0.1$ and $\Lambda = 1.0$. A 'frozen' main body is still present. Two smaller rounded voids have developed and are separated from the main body by thin filaments, which progressively narrow as the voids propagate away from the main body. An interesting question is whether the interface pinches off, leading to the formation of multiple voids possibly accompanied by dislocations formed during the pinch off event. Fig. 13 plots the width W of the neck at its thinnest point versus time. The figure shows that the neck width roughly decreases linearly in time for $t \geqslant 0.404$. For a fixed number of discretization points W eventually saturates to a fixed value (e.g., $W \sim 0.03$ for $N = 512$). However, closer
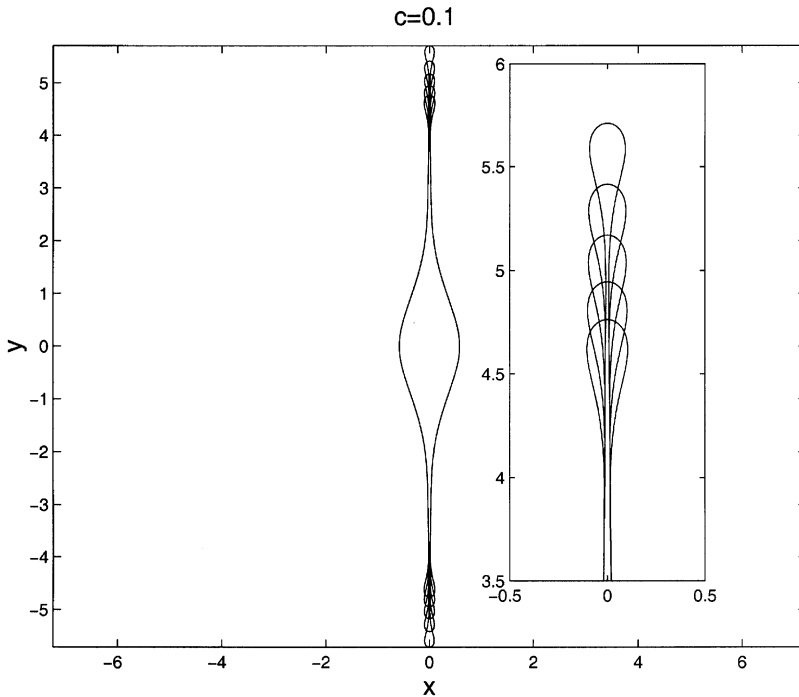
Fig. 12. Long time evolution of the solution for $\varepsilon = 0.08$, $\Lambda = 1.0$, $c = 0.1$, illustrating the trend towards pinch-off. The profiles are plotted at the times 0.4070–0.4078 in time increments of 0.0002. The inset gives details of the tip-streaming filament.

inspection shows that the neck width is equivalent to approximately 2–4 grid points at the time of saturation. Studies of the accuracy of boundary integral methods done within the context of fluid dynamics (Baker and Shelley, 1986) show that such methods typically lose accuracy when different portions of the interface approach to within a few discretization points. The behavior observed here is consistent with this study. After doubling the number of grid points and restarting the simulation from a point prior to saturation, the neck width continues to decrease at the prior (linear) rate, i.e., the saturation is delayed for a time. Although the ejected voids are slowly shrinking in time, the numerical evidence indicates that they will not shrink to zero area before pinch-off. In summary then, the evidence as presented in Fig. 13 is suggestive of the appearance of a topological singularity in finite time.

4.3. Wrinkling

The time-dependent simulations of Section 4.2.2 are limited in the extent which c can be reduced (or equivalently ε increased) for positive Λ, due to the numerically intensive operation of solving the elasticity problem when there is a large number of fast growing modes. Therefore, we consider here a particle evolving under anisotropic
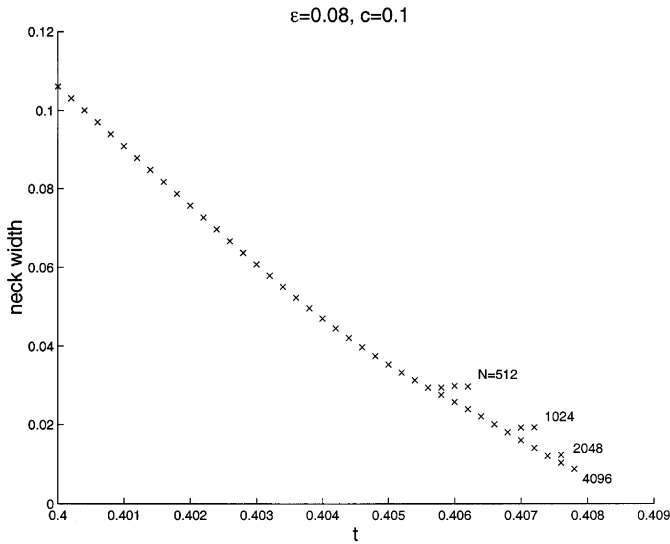
Fig. 13. Minimum neck width versus time during long time evolution. Parameter values are $\varepsilon = 0.08$ and $c = 0.1$. Results are shown for $N = 512$, 1024, 2048 and 4096 points.

surface energy only, i.e. with $\Lambda = 0$, for which a very small value of the regularization c can be implemented in the time-dependent simulations. The results here complement the steady-state calculations presented in Fig. 6 and show that the regularization gives the expected result (i.e., admissible angles) in a dynamic situation when $\Lambda = 0$. We note that these results are similar to calculations of the decomposition of an unstable planar interface into stable orientations (Liu and Metiu, 1993).

The result of a numerical simulation employing the arclength–angle method with $c = 0.001$ and $\varepsilon = 0.3$ is shown in Fig. 14. A very small time step, $\Delta t = 10^{-9}$, is necessary to adequately resolve the motion. This can be explained by the presence of very fast growing modes due to the large anisotropy and small regularization. Starting from an initially circular interface the void develops wrinkles at orientations corresponding to unstable directions in the zero regularization problem. The pattern coarsens over time; the figure shows a transition from a three crested pattern (repeated due to the bilateral symmetry) to one with two crests. The wrinkling is qualitatively similar to that shown in Eggleston et al. (2001), although we do not observe the retardation of motion at the most unstable orientations, as reported there.

The formation of wrinkles is qualitatively explained by appealing to linear theory. Consider a portion of the initially circular interface oriented at the unstable angle θ_0. Since the local interface is unstable, perturbations will grow, at least in a neighborhood of θ_0. Writing $\theta = \theta_0 + \tilde{\theta}$ and performing a 'frozen coefficient' linear analysis of Eqs. (29), (30) (i.e. where the frozen coefficient θ_0 is used in place of a more general function of α) shows that a(local) mode with wavenumber k will be unstable provided that $k < \sqrt{(15\varepsilon \cos 4\theta_0 - 1)/c}$. Wrinkling should occur in regions for which this
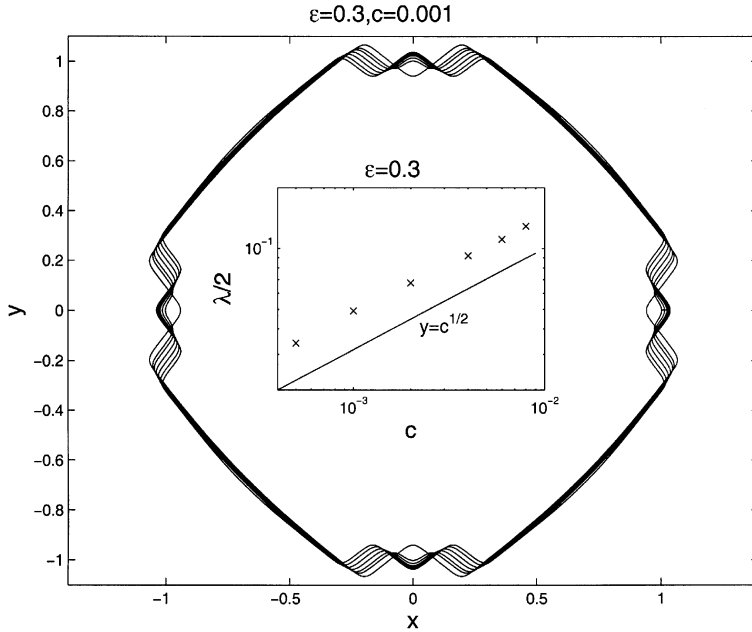
Fig. 14. Formation of wrinkles followed by coarsening. Parameter values are $\varepsilon = 0.3$, $c = 0.001$. First profile is at time $t = 0.0002$; time increment for plots is $\Delta t = 0.0004$, with the last two increments being $\Delta t = 0.0002$. Inset: computed half-wavelength ($\lambda/(2a)$) of small amplitude wrinkles plotted versus c, shown as a log–log plot. Here $\varepsilon = 0.3$. Shown for comparison is the curve $y = c^{1/2}$, which is a line of slope 1/2 in the figure.

inequality is satisfied for some $k \geqslant 1$. Additionally, the most unstable (non-dimensional) wavelength λ_m/a is given by

$$\frac{\lambda_m}{a} = \pi \sqrt{\frac{6c}{15\varepsilon \cos 4\theta_0 - 1}} \tag{36}$$

(see also Gurtin, 1993). Thus spatial patterns of wavelength λ_m/a should be most prevalent in the wrinkled interface.

Fig. 14 (inset) shows that this corresponds to what is observed in practice. The figure indicates the computed relationship between the wavelength of small amplitude wrinkles and the regularization c. The $c^{1/2}$ dependence embodied in (36) is exhibited by the data, as is apparent through comparison with the 'curve' $y = c^{1/2}$ (note the plot uses log–log coordinates).

Similar calculations for very small c and $\Lambda > 0$ are numerically expensive and therefore have not been considered. Nevertheless, one may extrapolate the above behavior to the case $\Lambda > 0$: the expectation is that for small enough c the interface would similarly wrinkle with local shape (near a corner) resembling the Wulff shape. Over longer times the influence of elasticity would become apparent and each corner would be susceptible to tip streaming.

5. Discussion and conclusions

We have considered the motion of voids in an elastic material in the presence of large anisotropy; the ill-posedness inherent in the usual models is regularized through the incorporation of explicit curvature dependence in the surface energy density γ. At small enough ratios of elastic energy to surface energy (i.e., small Λ) we find steady state profiles that appear to develop corners in the zero regularization limit. However, the emerging corner angles depend on the elastic energy and can differ from the angle predicted by the ($\Lambda = 0$) Wulff shape. This result is contrary to predictions of the angle based on a force balance at a true corner. In contrast, when $\Lambda = 0$ we find the emerging ($c \to 0$) corner angles correspond to the Wulff shape in both steady and dynamic situations.

The conclusion to be made from these results hinges on the question of what is the 'correct' physics to employ in the case of large anisotropy and $\Lambda \neq 0$, i.e., what is the correct physics at corners. We discuss the two main possibilities:

1. The correct physics requires the existence of corners with the Wulff angle (thus avoiding the ill-posed directions). In this case, one must proceed with care in applying other regularizations, e.g., those based on higher order terms such as considered here. In particular, only regularizations which yield the Wulff angle in the zero regularization limit would be desired.
2. The correct physics requires a regularization, such as one based on the incorporation of higher order terms in the governing equations. In this case one must be open to the possibility that the physically relevant corner angle, corresponding to the zero regularization limit, is different form the Wulff angle. This raises the additional possibility that the angle may depend on the specific nature of the regularization. If so, then it is critical to employ only physically based regularizations. Careful modeling (even at the atomic scale) may be required to obtain such regularizations.

There is another point of view worth discussing concerning steady states with the non-Wulff angles and it is related to the results presented in Fig. 5 for the dependence of Λ_c on c. As discussed earlier, our numerical results have implied that as c tends to zero, Λ_c tends to a positive number. The implication of this is that these steady states should be observable for any value of c as long as the applied strain is small enough. Notice that there is a rapid decrease in Λ_c as c tends to zero. Suppose that Λ_c actually does go to zero as c tends to zero. Then since c is expected to be small for most physical systems, it is likely that the applied strain in an experiment would be greater than the critical value, so a tip-streaming event would occur. From the behavior presented in Fig. 11, we would then expect the void to evolve into a shape where the Wulff angles are approximately satisfied except for a small region in the neighborhood of the actual corner. Hence an experiment would report that the Wulff angle is observed even for small applied strains.

In addition to the results summarized above, we also find that when Λ is sufficiently large that there are no longer steady-state solutions and the void continuously lengthens in a filamenting (tip-streaming) instability, eventually leading to a topological

singularity. Although we have been primarily interested in the nature of the zero regularization limit, our tip-streaming results may be compared to behavior in physical systems after obtaining a representative estimate for the value of c. The dimensional regularization c_1 measures how large a change in surface energy is possible for a given change in curvature (see Eq. (10)). A reasonable estimate allows for a 10% change in surface energy for a change in curvature of 0.1–1 nm. Using the representative value $\gamma_0 = 10^3$ ergs/cm^2, Eq. (10) then implies that 10^{-14} ergs $< c_1 < 10^{-12}$ ergs. This in turn is consistent with the estimate (Stewart and Goldenfeld, 1992) $c_1 = 10^{-13}$ ergs, using $c_1 = \gamma_0 d^2$ where $d = 10^{-8}$ cm is a (representative) lattice parameter. Through the definition of c, the dimensional quantity c_1 sets the length scale of the void. Thus if $c = 10^{-3}$ then the radius a of the void equals 10 nm, whereas if $c = 0.1$ then $a = 1$ nm, assuming $c_1 = 10^{-12}$ ergs. The width W of the channel that connects the tip-streaming void to the larger void is a small fraction of the void radius. Roughly, our numerics show that representative values at the *onset* of tip-streaming are $W \sim a$ for $c = 0.1$, $W \sim 0.1a$ for $c = 0.01$ and $W \sim 0.01a$ for $c = 0.001$. Thus W is approximately the radius of an atom (0.1 nm), and consequently the channels are extremely thin, if they exist at all. However, this may not be the case for some systems, i.e., those with relatively low surface energies (such as solid–solid interfaces and certain solid–liquid systems).

It is unclear if there is any experimental evidence for tip streaming. Recent experiments (J. Mirecki Millunchick, private communication) investigating the stability of stepped surfaces show structures with a similar morphology. These structures are a result of an instability occurring at the step face (terrace); the terrace evolves in such a way to create a cusplike interface pointing into the material (viewed from above the step) with a void connected at the 'tip' of the cusp. The lateral scale of this structure is much greater than its depth, suggesting that it is effectively a two-dimensional phenomenon. This rules out the Rayleigh-instability as a possible cause. However, it is not clear if the mechanism of formation is related to that considered here. In addition, the voids that are shed can be quite small leading to the possibility that these voids emit vacancies and thus dissolve into the matrix.

It has been hypothesized (Grilhe, 1993) that a mechanism analogous to tip streaming followed by topological singularity formation may be a way of creating dislocations by surface diffusion. The plausibility of creating a particular dislocation type (i.e., hollow dislocation core with a super Burgers vector) by this mechanism is discussed in Grilhe (1993), although neither quantitative theoretical nor experimental evidence for such a creation scenario is given. We mention here the plausibility of a somewhat different type of dislocation formation: namely that the rejoining of the channel surfaces at pinch-off is accompanied by a shift in atomic positions in a direction perpendicular to the xy plane, leading to a form of screw dislocation. Although this paper provides quantitative theoretical calculations suggesting the feasibility of such a mechanism in certain systems, we are aware of no experimental evidence for this particular type of dislocation formation. Other possible mechanisms for dislocation nucleation near a free surface cusp are reviewed in Gao and Nix (1999).

Conversely, dislocation nucleation may impede the tip-streaming process. Specifically, the non-dimensional stresses at the tip of a streaming filament are found to be

$O(10)$ for the values of c considered here. The dimensional stresses can be calculated from Eq. (14) using the representative values $E = 1.2 \times 10^{12}$ ergs/cm^3, $\Lambda = 1.0$ and $a = 10$ nm. This gives stresses of the order of 10^{10} ergs/cm^3. This stress is on the order of 0.01 E and thus is close to the stress thought to be necessary to nucleate dislocations (Hirth and Lothe, 1982). Thus, the formation of small voids at the tip may not occur if the stresses at the tip exceed that required to nucleate dislocations prior to the formation of the voids. In this case, the stresses will be relieved by dislocation formation and the driving force for streaming will be reduced (Hirth and Lothe, 1982).

As described, the tip-streaming phenomena observed in our calculations may be unphysical for systems with relatively high surface energies γ_0, due to the narrowness of the required channels. In this case the void evolution might 'stall' in a terminal steady profile not unlike that shown in Fig. 10 before the emission of the very thin filament. There is some experimental evidence for such morphologies in dislocation free films (J. Floro, private communication), but a quantitative comparison awaits further studies.

One difficulty in the current study involves modeling the curvature dependence of γ, i.e., Eq. (10). The truncation involved in obtaining this equation, i.e., keeping only up to κ^2 terms, is not formally valid when regions of high curvature develop. Nevertheless, we feel that the qualitative behavior uncovered using this expression is generic, i.e., independent of the details of the particular regularization. More physically realistic expressions for the dependence of γ on curvature require first principles calculation of the energy of a corner or edge, and this is a topic of future investigation.

Acknowledgements

References

Akaiwa, N., Thornton, K., Voorhees, P.W., 2001. Large scale simulations of microstructural evolution in elastically stressed solids. J. Comp. Phys. 173, 61–86.

Angenant, S., Gurtin, M.E., 1989. Multiphase thermodynamics with interfacial structure. 2. Evolution of an isothermal interface. Arch. Rat. Mech. Anal. 108, 323–391.

Arzt, E., Kraft, O., Nix, W., Sanchez, J., 1994. Electromigration failure by shape change of voids in bamboo lines. J. Appl. Phys. 76, 1563.

Asaro, R.J., Tiller, W.A., 1972. Interface morphology development during stress corrosion cracking: Part I. Via surface diffusion. Metall. Trans. 3, 1789–1796.

Baker, G.R., Shelley, M.J., 1986. Boundary integral techniques for multi-connected domains. J. Comp. Phys. 64, 112.

Burton, W.K., Cabrera, N., Frank, F.C., 1951. Trans. R. Soc. London 243, 299.

Ceniceros, H., Hou, T., 2000. The singular perturbation of surface tension in Hele–Shaw flows. J. Fluid Mech. 409, 251–272.

Chiu, C-H., Gao, H., 1993. Stress singularities along a cycloid rough surface. Int. J. Solids Struct. 30, 2983–3102.

Coriell, R.F., Sekerka, R.F., 1976. The effect of the anisotropy of surface tension and interface kinetics on morphological instability. J. Cryst. Growth 34, 157.

Di Carlo, A., Gurtin, M.E., Podio-Guidugli, P., 1992. A regularized equation for anisotropic motion-by-curvature. SIAM J. Appl. Math. 52 (4), 1111–1119.

Eggleston, J.J., McFadden, G.B., Voorhees, P.W., 2001. A phase-field model for highly anisotropic interfacial energy. Physica D 150, 91–103.

Freund, L.B., Jonsdottir, F., 1993. Instability of a biaxially stressed thin film on a substrate due to material diffusion over its free surface. J. Mech. Phys. Solids 41, 1245–1264.

Gao, H., 1991. A boundary perturbation analysis for elastic inclusions and interfaces. Int. J. Solids Struct. 28, 703–725.

Gao, H., 1992. Stress analysis of holes in anisotropic elastic solids: conformal mapping and boundary perturbation. Q. J. Mech. Appl. Math. 45, 149–168.

Gao, H., 1994. Some General Properties of Stress-Driven Surface Evolution in a Heteroepitaxial Thin Film Structure. J. Mech. Phys. Solids 42, 741–772.

Gao, H., 1995. The hypocycloid cavity: a path from a Griffith slit crack to a cusped cycloid surface. Proc. R. Soc. London 448, 465–483.

Gao, H., Nix, W.D., 1999. Surface roughening of heteroepitaxial thin films. Ann. Rev. Mater. Sci. 29, 173–209.

Gibbs, J.W., 1878. On the equilibrium of heterogeneous substances. In: Gibbs, J.W. (Ed.), The Scientific Papers, Vol. 1. Dover, New York, 1961.

Golovin, A.A., Davis, S.H., Nepomnyashchy, A.A., 1998. A convective Cahn–Hilliard model for the formation of facets and corners in crystal growth. Physica D 122, 202–230.

Greengard, L., Kropinski, M.C., Mayo, A., 1996. Integral equation methods for Stokes flow and isotropic elasticity in the plane. J. Comp. Phys. 125, 403–414.

Grilhe, J., 1993. Surface instabilities and dislocation formation at free surfaces. Europhys. Lett. 23, 141–146.

Grinfeld, M., 1986. Instability of the separation boundary between a nonhydrostatically stressed elastic body and melt. Sov. Phys. Dokl. 31, 831–834.

Gurtin, M.E., 1993. Thermomechanics of Evolving Phase Boundaries in the Plane. Oxford Press, Oxford.

Gurtin, M.E., Voorhees, P.W., 1998. On the effects of elastic stress on the motion of fully faceted interfaces. Acta Mater. 46, 2103–2112.

Herring, C., 1951. Surface tension as a motivation for sintering. In: Kingston, W.E. (Ed.), The Physics of Powder Metallurgy. McGraw Hill, New York.

Hirth, J.P., Lothe, J., 1982. Theory of Dislocations. Wiley, New York.

Hou, T.Y., Lowengrub, J.S., Shelley, M.J., 1994. Removing the stiffness from interfacial flows with surface tension. J. Comp. Phys. 114, 312.

Jesson, D.E., Pennycock, S.J., Baribeau, J.M., Houghton, D.C., 1993. Phys. Rev. Lett. 71, 1744.

Jou, H.-J., Leo, P.H., Lowengrub, J.S., 1997. Microstructural evolution in inhomogeneous elastic media. J. Comp. Phys. 131, 109.

Kessler, D.A., Koplik, J., Levine, H., 1987. Pattern selection in fingered growth phenomena. Adv. Phys. 37, 255–339.

Krasny, R., 1986. On singularity formation in a vortex sheet and the point vortex approximation. J. Fluid Mech. 167, 65–93.

Kutka, R.V., Freund, L.B., 1997. Minimum Energy Configuration of Epitaxial Material Clusters on a Lattice-Mismatched Substrate. J. Mech. Phys. Solids 45, 1835–1860.

Liu, F., Metiu, H., 1993. Dynamics of phase separation of crystal surfaces. Phys. Rev. B 48, 48–59.

Mikhlin, S.G., 1957. Integral Equations. Pergamon Press, New York.

Mullins, W.W., 1957. Theory of thermal grooving. J. Appl. Phys. 28, 333–339.

Mullins, W.W., 1962. J. Math. Phys. 3, 754.

Mullins, W.W., 1963. Solid surface morphologies governed by capillarity. In: Metal Surfaces. American Society for Metals, Metals Park, OH.

Muskhelishvili, N.I., 1953. Some Basic Problems in the Mathematical Theory of Elasticity. P. Noordhoff, Groningen.

Nozieres, P., 1992. Shape and growth of crystals. In: Godreche, C. (Ed.), Solids Far From Equilibrium. Cambridge University Press, Cambridge.

Ozkan, C.S., Nix, W.D., Gao, H., 1997. Appl. Phys. Lett. 70, 2247.

Press, W.H., Teukolsky, S.A., Vetterling, W.T., Flannery, B.P., 1992. Numerical Recipes. Cambridge University Press, Cambridge.

Saad, Y., Schultz, M., 1986. GMRES: a generalized minimum residual algorithm for solving nonsymmetric linear systems. SIAM J. Sci. Stat. Comp. 7, 856.

Shchukin, V.A., Bimberg, D., 1999. Spontaneous ordering of nanostructures on crystal surfaces. Rev. Mod. Phys. 71, 1125–1172.

Sidi, A., Israeli, M., 1988. Quadrature methods for periodic singular and weakly singular Fredholm integral equations. J. Sci. Comp. 3, 201.

Siegel, M., Tanveer, S., Dai, W., 1996. Singular effects of surface tension in evolving Hele–Shaw flows. J. Fluid Mech. 323, 201.

Spencer, B.J., 2003. Asymptotic solutions for the equilibrium crystal shape with small corner energy regularization. Preprint.

Spencer, B.J., Meiron, D.I., 1994. Nonlinear evolution of the stress-driven morphological instability in a two-dimensional solid. Acta. Metall. Mater. 42, 3629–3641.

Spencer, B.J., Tersoff, J., 1997. Equilibrium Shapes and Properties of Epitaxially Strained Solid Islands. Phys. Rev. Lett. 79, 4858–4861.

Spencer, B.J., Voorhees, P.W., Davis, S.H., 1991. Morphological instability in epitaxially strained dislocation free solid films. Phys. Rev. Lett. 67, 3696–3699.

Srolovitz, D.J., 1989. On the stability of surfaces of stressed solids. Acta Metall. 37, 621–625.

Srolovitz, D.J., Davis, S.H., 2001. Do stresses modify wetting angles. Acta Mater. 49, 1005–1007.

Stewart, J., Goldenfeld, N., 1992. Phys. Rev. A 46, 6505.

Suo, Z., Wang, W., 1994. Diffusive void bifurcation in stresses solid. J. Appl. Phys. 76, 3410–3421.

Voorhees, P.W., Coriell, S.R., McFadden, G.B., 1984. The effect of anisotropic crystal-melt surface tension on grain boundary groove morphology. J. Cryst. Growth 67, 425–440.

Wang, W., Suo, Z., 1997. Shape change of a pore in a stressed solid via surface diffusion motivated by surface and elastic energy variation. J. Mech. Phys. Solids 45, 709.

Xia, L., Bower, A.F., Suo, Z., Shih, C.F., 1997. A finite element analysis of the motion and evolution of voids due to strain and electromigration induced surface diffusion. J. Mech. Phys. Solids 45, 1473–1493.

Yang, W.H., Srolovitz, D.J., 1994. Surface morphology evolution in stressed solids: surface diffusion controlled crack initiation. J. Mech. Phys. Solids 42, 1551–1574.

Zhang, Y.W., Bower, A.F., 1999. Numerical Simulation of Island Formation in a Coherent Strained Epitaxial Thin Film System. J. Mech. Phys. Solids 42, 2273.